

1           **Modeling surface water and groundwater mixing and mixing-dependent**  
2                                   **denitrification with bedform dynamics**

3  
4                   Xue Ping<sup>1</sup>, Zhang Wen<sup>1,2\*</sup>, Yang Xian<sup>1</sup>, Menggui Jin<sup>1,2</sup>, Stefan Krause<sup>3</sup>

5  
6   Revised manuscript submitted to *Hydrology and Earth System Sciences*

7  
8   <sup>1</sup>Hubei Key Laboratory of Yangtze Catchment Environmental Aquatic Science, School of  
9   Environmental Studies, China University of Geosciences, Wuhan, China

10   <sup>2</sup>State Key Laboratory of Biogeology and Environmental Geology, China University of  
11   Geosciences, Wuhan, China

12   <sup>3</sup>School of Geography, Earth and Environmental Sciences, University of Birmingham, UK

13  
14   \*Corresponding author: Zhang Wen ([wenz@cug.edu.cn](mailto:wenz@cug.edu.cn))

16 **Notation**

$S$	Stream slope [-]
$H$	Water depth [L]
$U$	Stream velocity [L T <sup>-1</sup> ]
$\lambda$	Ripple wavelength [L]
$u_c$	Bedform migration celerity [L T <sup>-1</sup> ]
$l$	Streambed height [L]
$H_d$	Ripple height [L]
$B$	Riverbed per unit width [L]
$D_{50}$	Median sediment size [L]
$x$	Horizontal coordinate, rightward positive [-]
$y$	Vertical coordinate, upward positive [-]
$k$	Sediment permeability [L <sup>2</sup> ]
$K$	Sediment hydraulic conductivity [L T <sup>-1</sup> ]
$h$	Hydraulic head [L]
$h_m$	Amplitude of the sinusoidal head variation [L]
$m$	Wavenumber of the variation [-]
$g$	Gravity acceleration [L T <sup>-2</sup> ]
$c_i$	Concentration of reactive components [M L <sup>-3</sup> ]
$c_{gw}$	Groundwater tracer [M L <sup>-3</sup> ]
$v$	Seepage velocity [L T <sup>-1</sup> ]
$v_i$	Seepage velocity in the $i$ -direction [L T <sup>-1</sup> ]

$v_j$	Seepage velocity in the $j$ -direction [ $L T^{-1}$ ]
$\theta$	Sediment porosity [-]
$\alpha_L$	Longitudinal dispersivity [L]
$\alpha_T$	Transverse dispersivity [L]
$D_{ij}$	Hydrodynamic dispersion [ $L^2 T^{-1}$ ]
$D_m$	Molecular diffusion coefficient [ $L^2 T^{-1}$ ]
$\tau$	Tortuosity factor [-]
$V_{AR}$	Maximum reaction rate of aerobic respiration [ $T^{-1}$ ]
$V_{DN}$	Maximum reaction rate of denitrification [ $T^{-1}$ ]
$K_{inh}$	Non-competitive inhibition factor [ $M L^{-3}$ ]
$K_{DOC}$	Half-saturation for dissolved organic carbon [ $M L^{-3}$ ]
$K_{NO_3^-}$	Half-saturation for nitrate [ $M L^{-3}$ ]
$K_{O_2}$	Half-saturation for oxygen [ $M L^{-3}$ ]
$X_{AR}$	Microbial concentration facilitating aerobic respiration [ $M L^{-3}$ ]
$X_{DN}$	Microbial concentration facilitating denitrification [ $M L^{-3}$ ]
$\rho_s$	Sediment density [ $M L^{-3}$ ]
$\rho$	Water density [ $M L^{-3}$ ]
$P$	Hydraulic pressure [ $M L^{-1} T^{-2}$ ]
$D^*$	Dimensionless particle parameter [-]
$u^*$	Bed shear velocity [ $L T^{-1}$ ]
$u_{cr}^*$	Critical bed shear velocity [ $L T^{-1}$ ]
$n$	Manning coefficient [-]

$\tau^*$	Shield parameter [-]
$\tau_{cr}$	Critical shear stress [ $M L^{-1}T^{-2}$ ]
$\tau_{cr}^*$	Critical Shield parameter [-]
$r$	Submerged specific gravity of sediment [-]
$R_{O_2}$	Aerobic respiration rate [ $M L^{-3}T^{-1}$ ]
$R_{S-NO_3}$	Non-mixing-dependent denitrification rate [ $M L^{-3}T^{-1}$ ]
$R_{g-NO_3}$	Mixing-dependent denitrification rate [ $M L^{-3}T^{-1}$ ]
$R_{DOC}$	Dissolved oxygen carbon consumption rate [ $M L^{-3}T^{-1}$ ]
$\nu$	Kinematic viscosity of water [ $L^2 T^{-1}$ ]
$\mu$	Dynamic viscosity of water [ $M L^{-1} T^{-1}$ ]
$u_s$	Underflow seepage velocity induced by stream gradient [ $L T^{-1}$ ]
$Re$	Reynolds number [-]
$U_r$	ratio of bedform celerity to pore water velocity [-]
$u_p$	Darcy velocity induced by pumping process [ $L T^{-1}$ ]
$u_q$	Vertical groundwater flux [ $L T^{-1}$ ]
$U_b$	Ratio of vertical groundwater flux to hyporheic exchange flux
$\tau_R$	Biogeochemical reaction timescale [T]
$\tau_T$	Water transport timescale [T]
$Da$	Damköhler number [-]
$\Delta x$	Bedform migrating displacement per timestep (L)
$dt$	The length of per timestep (T)
$Da'$	Conversion factor for unit Darcy to $m^2$ [-]

$F_{mix}$	Proportion of mixing flux to hyporheic exchange flux [-]
$A_{mix}$	Proportion of mixing zone to the whole domain [-]
$A$	Streambed area [ $L^2$ ]
$M_{NDN}$	Nitrate removed by non-mixing-dependent denitrification [ $M T^{-1}$ ]
$M_{DN}$	Nitrate removed by mixing-dependent denitrification [ $M T^{-1}$ ]
$N_{RE}$	Nitrate removal efficiency [-]
$M_{in}$	Nitrate being introduced into streambed [ $M T^{-1}$ ]
$F_{in}$	Oxygen influx [ $M L^{-2} T^{-1}$ ]
$F_{out}$	Oxygen outflux [ $M L^{-2} T^{-1}$ ]
$A_o$	Oxygenated area [ $L^2$ ]

#### Abbreviations

HZ	Hyporheic zone
SW	Surface water
GW	Groundwater
HEF	Hyporheic exchange flow
MF	Mixing flux
NMD	Non-mixing-dependent
MD	Mixing-dependent
AR	Aerobic respiration
DN	Denitrification
RMSE	Root means square error

DNRA          Dissimilatory nitrate reduction to ammonium

ANAMMOX     Anaerobic ammonium oxidation

18 **Abstract** The hyporheic zone (HZ), where surface water (SW) and groundwater (GW) interact  
19 and mix, acts as a critical interface that attenuates contaminants through enhanced  
20 biogeochemical cycling. While bedform migration significantly influences hyporheic exchange  
21 and non-mixing-driven reactions of solutes from upstream SW, the effects of bedform migration  
22 on SW-GW mixing dynamics and mixing-triggered biogeochemical reactions—particularly  
23 under gaining stream conditions—remain poorly understood. Establishing a coupled  
24 hydrodynamic and reactive transport model that incorporates bedform migration, this paper  
25 systematically examines nitrogen processing for scenarios of variable sediment grain size,  
26 stream velocities, and upwelling GW fluxes. Results of this study reveal that SW-GW mixing  
27 and mixing-triggered denitrification zones progressively transition from crescent shapes into  
28 uniform band-like configurations as bedforms migrate. Both hyporheic exchange flux and  
29 mixing flux increase with increasing stream velocity and associated bedform celerity. The  
30 mixing proportion and mixing zone size increase at the start of migration, while they reach  
31 approximately stable when turnover becomes the dominant hyporheic exchange mechanism.  
32 Slow to moderate migrated bedforms with enhanced mixing dynamics facilitate mixing-  
33 triggered denitrification, whereas fast stream flows and migrating bedforms shorten solute  
34 residence timescales and limits denitrification potential. Consequently, in fine to medium sandy  
35 sediments, groundwater-borne nitrate removal efficiency declines significantly with bedform  
36 migration. The self-purification capacity of the HZ, and particularly its functioning as a natural  
37 barrier against GW contamination, is hindered under such dynamic bedform conditions. These  
38 findings highlight the need to maintain stable bedform conditions in restoration projects to  
39 enhance the capacity of HZ contaminant attenuation.

## 40 **1. Introduction**

41 Anthropogenic activities such as the intensification of agricultural practices with its  
42 increased used of mineral and organic fertilizers, together with high livestock densities and  
43 emissions of inadequately treated domestic and industrial wastewater have significantly  
44 increased nitrogen loading to rivers and groundwater, which impacts water quality, causing  
45 eutrophication, hypoxic and related deterioration of ecosystem functions (Conley et al., 2009;  
46 Rouse et al., 1999). Long-term regulatory monitoring data (e.g., from the UK) indicate that  
47 nitrate levels have stabilized in many rivers, while nitrate concentrations in groundwater-fed  
48 rivers continue to increase (Burt et al., 2011; Howden and Burt, 2008). The persistence of nitrate  
49 contamination in groundwater and associated risks of a “nitrate time bomb” (Ascott et al., 2019)  
50 has highlighted the urgency of exploring the potential of natural microbial processes to mediate  
51 nitrate transformation and removal in riverbed sediments (Shelley et al., 2017; Lansdown et al.,  
52 2015; Rivett et al., 2008).

53 The hyporheic zone (HZ) has received significant attention for its potential to facilitate  
54 enhanced nitrate transformation and removal via denitrification that is a primary process  
55 permanently reducing nitrate, with hyporheic exchange flows (HEFs) acting as a critical  
56 mechanism for transporting nitrate-rich surface water to the riverbed sediments where microbial  
57 activities and biogeochemical reaction rates are enhanced (Boano et al., 2014; Boulton et al.,  
58 1998; Cardenas, 2015; Xian et al., 2022; Krause et al., 2022). It has for long been assumed that  
59 predominantly stream waters provide inputs of bioavailable (mainly dissolved) organic carbon  
60 (DOC), oxygen ( $O_2$ ) and nitrate ( $NO_3^-$ ) into the riverbed where the residence and reaction times  
61 determine the occurrence of aerobic respiration and the potential for shifts into anaerobic

62 conditions that may facilitate denitrification along the HEF paths in the presence of enough  
63 remaining DOC (Zarnetske et al., 2011a, b). These hydrological and biogeochemical  
64 mechanisms are in this form mainly representative of headwater streams, where the HEF is  
65 induced by stream flow turbulence (Boano et al., 2011; Roche et al., 2018, 2019), local  
66 geomorphological setting (Cardenas et al., 2008; Marzadri et al., 2012; Tonina and Buffington,  
67 2007), and flow obstacles such as woody debris, streambed engineering or restoration structures  
68 (Briggs et al., 2013; Wondzell et al., 2009), and hyporheic nitrate removal processes expected to  
69 mainly occur at the middle to end- hyporheic flow paths within HEF cell sediments.

70 In lowland systems, groundwater-fed streams and rivers in permeable catchments will be  
71 dominated by base flow of often nitrate enriched groundwaters. The subsurface hydrological  
72 conditions are driven by horizontal HEF as well as vertical fluxes resulting from regional  
73 groundwater flow toward (or from) the stream. Spatial variability in regional groundwater flow  
74 can significantly affect hyporheic exchange and biogeochemical cycling (Boano et al., 2013;  
75 Krause et al., 2013; Munz et al., 2011; Naranjo et al., 2015). It is important to note that the  
76 groundwaters of many piedmont plains and lowlands are often contaminated with high nitrate  
77 concentrations, but usually low in bio-available DOC (Krause et al., 2022). When nitrate-rich  
78 groundwater upwells through deeper sediments and reaches a region enriched in availability of  
79 DOC, nitrate reduction processes are significantly facilitated in the condition (Krause et al.,  
80 2009; Naranjo et al., 2015; Ping et al., 2023; Trauth et al., 2017). Stelzer and Bartsch (2012)  
81 developed such a conceptual framework of nitrate-rich gaining fluvial setting from 8 sites in the  
82 Waupaca River Watershed with three order magnitude in groundwater nitrate concentration.  
83 Lansdown et al. (2014) also measured high denitrification rate at deep sediment in the coarse-

84 grained sediments typical of groundwater-fed system, located within the River Leith (Cumbria,  
85 UK) where diverse nitrogen concentration changes were confirmed earlier (Krause et al., 2009).

86 Turnover and removal of the large amounts of  $\text{NO}_3^-$  from groundwater require DOC either  
87 from autochthonous streambed sources or from downwelling surface water to stimulate nitrate  
88 reduction (Krause et al., 2013, 2022; Ping et al., 2023; Sawyer, 2015; Trauth et al., 2017). For  
89 coarse grain or sandy riverbeds with low autochthonous organic matter content, stream-borne  
90 DOC dominates the supply of carbon sources for nitrogen transformation processes. Sandy  
91 sediments with less autochthonous organic carbon sources covering the majority of alluvial  
92 riverbeds are commonly characterized by topographical features such as ripples, dunes, and  
93 riffle-pool sequenced. The typical and multiple HEF cells induced by bedform topography are  
94 generally in crescent shapes (Fox et al., 2014; Wu et al., 2024). The downward advection of  
95 stream borne DOC provides electron donor and mixes with nitrate-rich and anoxic groundwater.  
96 It has been shown that the highest potential for mixing triggered denitrification is often found at  
97 the margin of the HEF cells, which represents the last natural protection before nitrate enter a  
98 stream (Hester et al., 2013, 2014; Gu et al., 2008; Nogueira et al., 2022). The effects of mixing  
99 triggered denitrification on groundwater borne nitrate transformation in HZs have been studied  
100 almost exclusively for the case of stationary, that is immobile bedforms (Hester et al., 2017,  
101 2019; Trauth and Fleckenstein et al., 2017; Ping et al., 2023).

102 Bedforms are mobile in dynamic equilibrium or undergo constant changes during periods  
103 of moderate to high stream flow, and they are typically found in medium and larger waterways  
104 under realistic field conditions (Bartholdy et al., 2015; Risse-Buhl et al., 2023; Schindler et al.,  
105 2015). For example, Harvey et al. (2012) observed the migrating bedforms of dunes (with a

106 median grain size  $D_{50}$  of 380  $\mu\text{m}$  for the riverbed sediments) at a velocity of 57.6 cm/h during  
107 base flow in the “Clear Run” stream in eastern North Carolina, USA. Ahmerkamp et al. (2017)  
108 found that the ripple bedforms for sands ( $D_{50} = 63 \mu\text{m}$ ) ranged from 11 to 29 cm with a constant  
109 ratio of bedform height and length at 1/9, and migrated at velocities of 0.7–6.5 cm/h in the  
110 German Bight, Southeastern part of the North Sea. Bedforms migration complicates the  
111 development of hyporheic flow fields, facilitates solute exchange, alters redox conditions in  
112 riverbeds, and affects contaminant transport and transformation (Ahmerkamp et al., 2015;  
113 Schulz et al., 2023; Peleg et al., 2024). Previous studies focused on ripple-driven hyporheic  
114 exchange in headwater to midstream reaches under neutral conditions, and simulated bedform  
115 migration via a moving frame of reference (Ahmerkamp et al., 2015; Jiang et al., 2022; Kessler  
116 et al., 2015; Zheng et al., 2019). Ping et al. (2022) used a fixed reference frame and noted that  
117 bedform migration negatively impacts non-mixing-dependent denitrification rates and stream-  
118 borne nitrate removal efficiency. However, no studies have yet investigated the effects of  
119 bedform migration on surface water-groundwater mixing in the lowland reaches of streams  
120 under gaining conditions, nor have they explored its controls or implications for mixing-induced  
121 denitrification in groundwater-fed streams and rivers.

122 In this study, numerical modeling of hyporheic flow and multi-component solute (DOC,  
123  $\text{O}_2$ , and  $\text{NO}_3^-$ ) transport is used to evaluate the effect of bedform migration on mixing-  
124 dependent denitrification in the HZ of a gaining river, where the overlying stream water is  
125 induced into the sediment by ripple-type bedforms. The objectives of this study are to determine  
126 the effects of bedform migration on the overall extent and magnitude of mixing of surface water

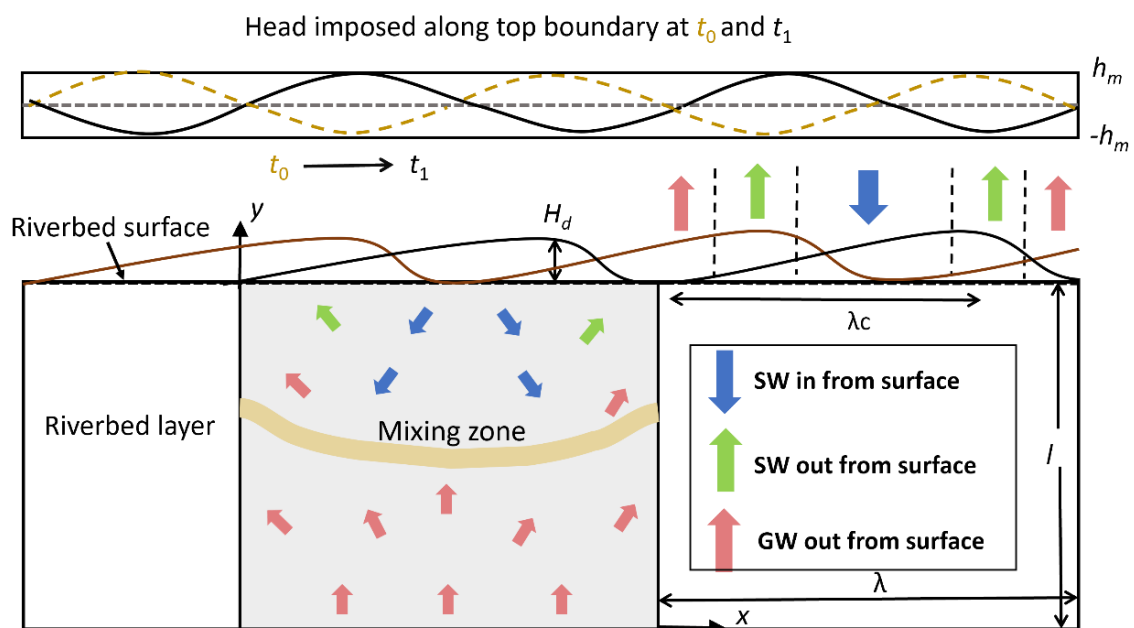
127 and upwelling groundwater, as well as its influences on groundwater-borne nitrate transport and  
128 transformation.

## 129 **2. Methods**

### 130 **2.1 Model description**

131 The stream flow over the bedform generates head gradients along the riverbed surface,  
132 drives hyporheic exchange, and induces the formation of periodic ripples. Ripples develop and  
133 migrate downstream above the riverbed surface as a consequence of bedload transport, with  
134 sediment grain eroded and deposited at the surface, whereas deeper streambed sediments remain  
135 relatively stable (Harvey et al., 2012; Precht et al., 2004). From the perspective of an observer  
136 who stands at the target single riverbed and watches the ripples passing by, the bedform shapes  
137 and associated pressure profiles migrate downstream over the immobile riverbed layer. Because  
138 ripple heights ( $H_d = 2$  cm) accounts for 20% of the stream water depth ( $H = 10$  cm) and are far  
139 smaller than that of the underlying immobile domain ( $l = 16$  cm), the undulating riverbed can be  
140 reasonably approximated as a flat bed with time-varying pressure patterns during bedform  
141 migration. Besides, reactive solute transport also primarily takes places within the immobile  
142 riverbed sediment. Therefore, a two-dimensional (2D) rectangular domain is constructed with a  
143 length ( $\lambda$ ) of 0.2 m and depth ( $l$ ) of 0.16 m. A fixed reference frame is adopted, with its origin  
144 located at the bottom-left corner of the model. Here, the horizontal direction corresponds to the  
145  $x$ -axis and the vertical direction to the  $y$ -axis. The model domain has four corners: A (0, 0), B (0,  
146  $l$ ), C ( $\lambda$ ,  $l$ ), and D ( $\lambda$ , 0). The lateral boundaries are AB (left,  $x = 0$ ) and CD (right,  $x = \lambda$ ); the top  
147 boundary is BC ( $y = l$ ), and the bottom boundary is AD ( $y = 0$ ).

148 The model schematic is sketched in Figure 1. The model is relevant to the model used by  
 149 Ping et al. (2022) but with significant differences. Specifically, Ping et al. (2022) focused on  
 150 ripple-driven hyporheic exchange processes in the headwater to midstream sections of streams  
 151 under neutral conditions. In contrast, the present study focuses on the downstream sections of  
 152 rivers under gaining conditions, aiming to simulate surface water-groundwater interacting and  
 153 mixing processes under dynamic bedforms. To our knowledge, previous migrating ripple models  
 154 have extensively examined surface water-groundwater interaction processes (i.e., ripple-driven  
 155 hyporheic exchange processes), yet the mixing process remains uninvestigated (Ahmerkamp et  
 156 al., 2017; Jiang et al., 2022; Zheng et al., 2019; Kessler et al., 2015). In downstream sections,  
 157 groundwater is typically nitrate-contaminated, and denitrification is often co-regulated by both  
 158 mixing regimes. The model is also developed with advancements of these previous models by  
 159 including an important biogeochemical reaction in nitrate dynamics, that is mixing-triggered  
 160 denitrification (see next section for details).



161  
 162 **Figure 1.** Schematic of the model domain with bed form geometry. Stream flow and bedform

163 migration are from left to right. The dashed yellow lines represent the streambed surface and  
164 head profile at time  $t_0$ , and the solid black lines represent the streambed surface and head profile  
165 after migration at  $t_1$ . “SW in” is where surface water enters the riverbed layer, “SW out” is  
166 where surface water discharges to the stream, and “GW out” is along the upstream and  
167 downstream sides of bedforms where groundwater discharges to the stream. The yellow band  
168 represents the mixing zone of surface water and groundwater. NMD reaction = non-mixing-  
169 dependent reaction and MD reaction = mixing-dependent reaction. This figure is modified from  
170 Figure 2 in Ping et al. (2022), with permission granted by Wiley.

171 In this study, hyporheic flow, multi-component solutes ( $\text{DOC}$ ,  $\text{O}_2$ , and  $\text{NO}_3^-$ ) transport, and  
172 biogeochemical reactions (both non-mixing-dependent NMD and mixing-dependent MD  
173 reactions) are modelled in saturated sediments beneath a riverbed layer. Stream flow over the  
174 riverbed is not simulated. The hyporheic exchange flow is driven by pumping (overlying flow  
175 over the bed form produces a pressure head  $h|_{y=l}$ ) and bedform migration (triangular shaped  
176 ripples migrate downstream by an average velocity  $u_c$ ) and influenced by upwelling  
177 groundwater. Stream water transports  $\text{DOC}$ ,  $\text{O}_2$ , and  $\text{NO}_3^-$  into the riverbed, whereas  
178 groundwater polluted with  $\text{NO}_3^-$  upwells toward the stream. In order to distinguish NMD and  
179 MD denitrification, we define stream-borne nitrate (s- $\text{NO}_3^-$ ) and groundwater-borne nitrate (g-  
180  $\text{NO}_3^-$ ) as two distinct reactants.

## 181 **2.2 Model formulation**

### 182 2.2.1 Governing equation

183 The pore water flow was calculated using Darcy’s law and the groundwater flow equation:

184 
$$\nabla \cdot (-K \nabla h) = 0 \quad (1)$$

185 where  $h$  [L] is the pressure head, and  $K$  [ $L T^{-1}$ ] =  $k\rho g/\mu$  is the hydraulic conductivity,  $k$  [ $L^2$ ] is the  
 186 permeability of the riverbed,  $\rho$  [ $M L^{-3}$ ] are the density of water,  $g$  [ $L T^{-2}$ ] is the gravity  
 187 acceleration, and  $\mu$  [ $M L^{-1} T^{-1}$ ] is the dynamic viscosity of water.

188 The transport of reactive solutes within the streambed sediment was described by the  
 189 advection-dispersion-reaction equation:

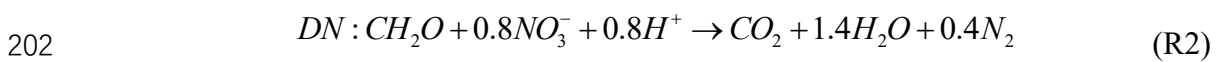
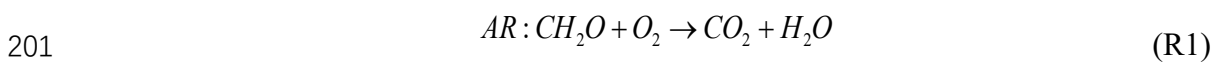
190 
$$\frac{\partial c_i}{\partial t} - \nabla \cdot (D_{ij} \nabla c_i) + \nabla \cdot (\mathbf{v} c_i) = R_i \quad (2)$$

191 where  $c_i$  [ $M L^{-3}$ ] represents the concentration of reactive components,  $\mathbf{v}$  [ $L T^{-1}$ ] is the seepage or  
 192 linear pore water velocity vector,  $D_{ij}$  [ $L^2 T^{-1}$ ] is the hydrodynamic dispersion tensor, and  $R_i$  [ $M$   
 193  $L^{-3} T^{-1}$ ] denotes the biogeochemical rate of reactive components; the elements of the dispersion  
 194 tensor  $D_{ij}$  are defined by Bear and Verruijt (1998):

195 
$$D_{ij} = (\alpha_L - \alpha_T) \cdot \frac{v_i v_j}{|\mathbf{v}|} + \delta_{ij} \cdot (\alpha_T |\mathbf{v}| + \theta \cdot \iota D_m) \quad (3)$$

196 where  $\alpha_L$  [L] and  $\alpha_T$  [L] are longitudinal and transverse dispersivities, respectively,  $D_m$  [ $L^2 T^{-1}$ ] is  
 197 molecular diffusion coefficient,  $v_i$  and  $v_j$  denote the seepage velocities in the  $i$ -direction and  $j$ -  
 198 direction, respectively; and  $\iota$  [-] is tortuosity.

199 The biogeochemical reactions: aerobic respiration (AR), non-mixing-dependent, and  
 200 mixing-dependent denitrification (DN) are considered in the reactive transport model:



203 Equations R1 and R2, with DOC as the electron donor and O<sub>2</sub> and NO<sub>3</sub><sup>-</sup> as sequential  
 204 electron acceptors, capture the primary mechanism of NO<sub>3</sub><sup>-</sup> cycling and are widely used in  
 205 studies on hyporheic zone nitrogen dynamics (Bardini et al., 2012; Hester et al., 2019; Zheng et  
 206 al., 2019). Denitrification is the well-recognized critical process for NO<sub>3</sub><sup>-</sup> transformation and  
 207 reduction in riparian and hyporheic zones. The reaction stoichiometry and electron acceptor  
 208 utilization order in R1 and R2 match well-established principles from lab incubations and field  
 209 investigations (Hedin et al., 1998; Liu et al., 2017; Zarnetske et al., 2011a, 2011b). Dissimilatory  
 210 nitrate reduction to ammonium (DNRA) and anaerobic ammonium oxidation (ANAMMOX) are  
 211 not included in the model, as these processes play secondary role on nitrogen cycling and  
 212 require highly specific conditions to occur (Zarnetske et al., 2012). Ammonia (NH<sub>4</sub><sup>+</sup>) was  
 213 excluded, as it is unstable in the study environment: NH<sub>4</sub><sup>+</sup> in surface water or groundwater is  
 214 prone to nitrification (converting NH<sub>4</sub><sup>+</sup> to NO<sub>3</sub><sup>-</sup>) either within hyporheic flow cells or in  
 215 upwelling groundwater upon O<sub>2</sub> exposure, leading to relatively low NH<sub>4</sub><sup>+</sup> concentrations (Hester  
 216 et al., 2014).

217 Reaction rates were defined using Monod kinetics (Monod, 1949):

$$218 \quad R_{AR} = V_{AR} \times X_{AR} \times \frac{c_{O_2}}{c_{O_2} + K_{O_2}} \times \frac{c_{DOC}}{c_{DOC} + K_{DOC}} \quad (4)$$

$$219 \quad R_{DN} = V_{DN} \times X_{DN} \times \frac{c_{NO_3^-}}{c_{NO_3^-} + K_{NO_3^-}} \times \frac{c_{DOC}}{c_{DOC} + K_{DOC}} \frac{K_{inh}}{K_{inh} + c_{O_2}} \quad (5)$$

220 The reaction terms  $R_i$  was given by

$$221 \quad R_{s-NO_3^-} = -R_{DN}(c_{s-NO_3^-}) \quad (6)$$

222 
$$R_{g-NO_3^-} = -R_{DN}(c_{g-NO_3^-}) \quad (7)$$

223 
$$R_{O_2} = -R_{AR} \quad (8)$$

224 
$$R_{DOC} = -R_{AR} - 0.8 \times (R_{DN}(c_{s-NO_3^-}) + R_{DN}(c_{g-NO_3^-})) \quad (9)$$

225 where  $V_{AR}$  and  $V_{DN}$  [ $T^{-1}$ ] are the maximum reaction rate of AR and DN,  $X_{AR}$  and  $X_{DN}$  [ $M L^{-3}$ ] are  
 226 the biomass of functional microbial groups facilitating the reaction components of AR and DN.  
 227  $K_{inh}$  [ $M L^{-3}$ ] is a non-competitive inhibition factor used for representing inhibition of DN given  
 228 oxygen availability.

### 229 2.2.2 Boundary condition

230 The pressure head imposed along the top boundary was described as a sinusoidal function  
 231 that moves downstream by the ripple migration velocity ( $u_c$  [ $L T^{-1}$ ]; Boano et al., 2013):

232 
$$h|_{y=l} = h_m \cdot \sin m(x - u_c dt) \quad (10)$$

233 where  $m$  [-] is the wave number of the variation ( $m = 2\pi/\lambda$ ),  $dt$  [T] denotes a timestep in the  
 234 simulation, and  $h_m$  [L] is the amplitude of the head variation (Elliott and Brooks, 1997):

235 
$$h_m = a \frac{U^2}{2g} \left( \frac{H_d / H}{0.34} \right)^e \quad (11)$$

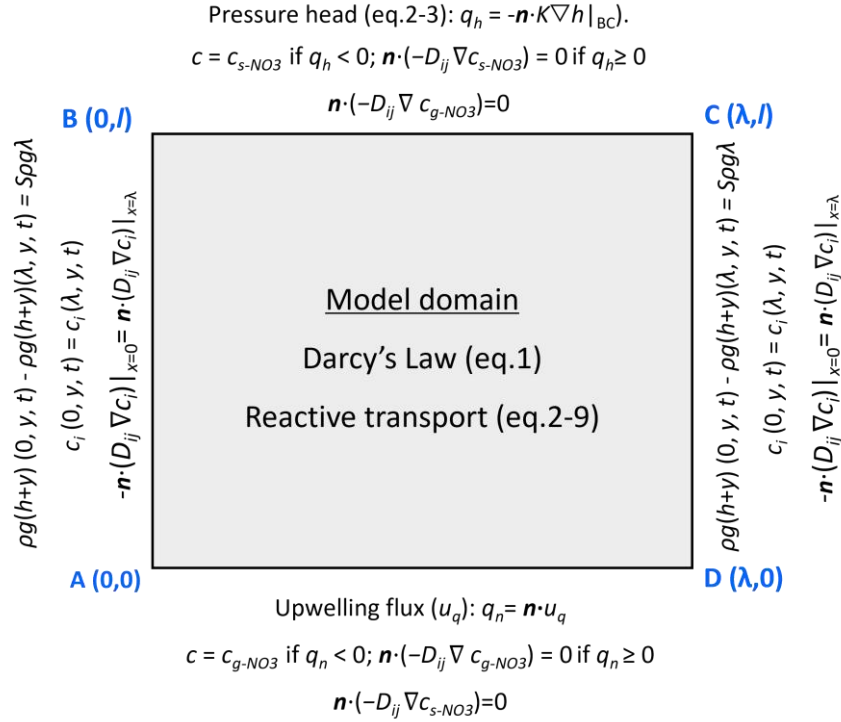
236 where  $a = 0.28$  [-] is a dimensionless coefficient,  $U$  [ $L T^{-1}$ ] is the average stream velocity,  $H_d$  [L]  
 237 is the height of the ripple,  $H$  [L] is the water depth. The exponent  $e$  equals to  $3/8$  if  $H_d < 0.34H$   
 238 and  $3/2$  otherwise. Given the periodic characteristics typically observed in riverbeds under field  
 239 conditions (Ahmerkamp et al., 2017; Harvey et al., 2012), a single ripple was chosen in this  
 240 study. Quasi-periodic pressure and periodic solute boundary conditions were applied to side  
 241 boundaries AB and CD to replicate the repetitive geometric constraints of the streambed. This is

242 a well-established practice in hyporheic exchange modeling, as it minimizes edge effects  
243 without the need for computationally intensive full-scale simulations of multiple consecutive  
244 bedforms:

$$245 \quad P(0, y, t) = P(\lambda, y, t) + \Delta P \quad (12)$$

$$246 \quad c_i(0, y, t) = c_i(\lambda, y, t) \quad \mathbf{n} \cdot (-D_{ij} \nabla c_i) \Big|_{x=0} = \mathbf{n} \cdot (D_{ij} \nabla c_i) \Big|_{x=\lambda} \quad (13)$$

247 where  $P$  [ $M L^{-1} T^{-2}$ ] is the pressure calculated using the hydrostatic head from equation (10) and  
248 elevation,  $P = \rho g(h+y)$ . The additional pressure drop  $\Delta P$  [ $M L^{-1} T^{-2}$ ] was derived from the  
249 streambed gradient and calculated using  $\Delta P = S \rho g \lambda$ . For the validation of model generalization,  
250 simulation of three consecutive ripples was conducted. The middle ripple was focused on to  
251 compare its vertical boundary-related pressure and solute concentration with outcomes from the  
252 single-ripple model. Simultaneously, comparisons were made between the two models (single-  
253 ripple and three-consecutive-ripple) regarding simulated riverbed flow fields, nitrate plumes,  
254 influxes, and reaction rates. Although moderate left/right boundary pressure differences were  
255 detected between their simulation results, such variations had negligible effects on reactive  
256 solute transport. This comparison is provided in the Supporting Information (Text S2).



257

258 **Figure 2.** Schematic diagram of the simulated domain and boundary conditions.

259 At the bottom boundary, an upward groundwater flux was defined to mimic the process of  
 260 groundwater discharge. For groundwater borne nitrate, the bottom boundary was specified as an  
 261 open Dirichlet boundary with constant g-NO<sub>3</sub><sup>-</sup> concentration in groundwater:

$$262 \quad \begin{cases} c = c_i & \mathbf{n} \cdot \mathbf{v} < 0 \\ \mathbf{n} \cdot (-D_{ij} \nabla c_i) = 0 & \mathbf{n} \cdot \mathbf{v} \geq 0 \end{cases} \quad (14)$$

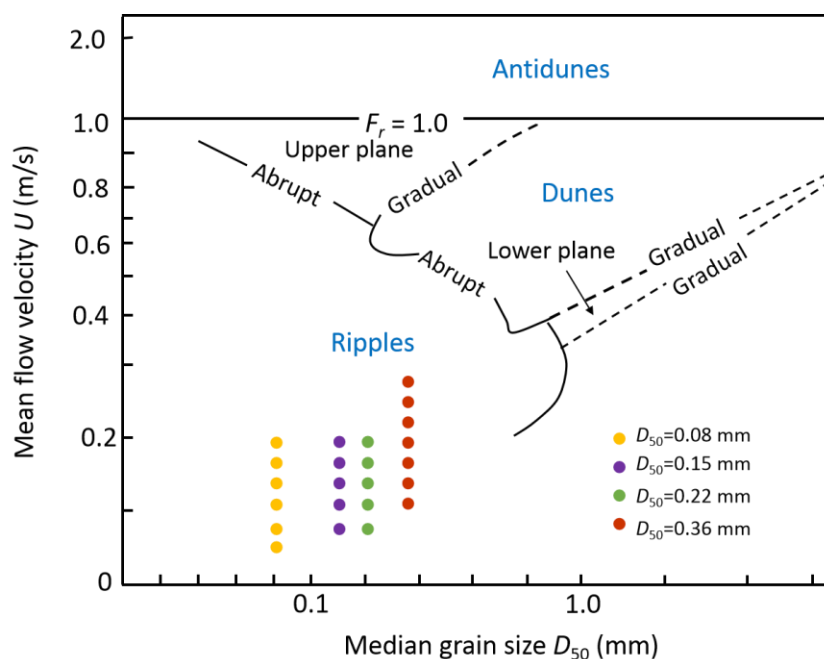
263 where the outward unit normal is  $n$ . Besides, the top boundary for the g-NO<sub>3</sub><sup>-</sup> was assigned as  
 264 outflow condition.

265 For stream-borne solutes includes DOC, O<sub>2</sub>, and s-NO<sub>3</sub><sup>-</sup>, an open boundary with a constant  
 266 solute concentration was imposed on the top boundary, and outflow boundary was applied on  
 267 the bottom of the domain. The concentrations of the all solutes were initially assumed to be  
 268 zero. A quantitative mass-balance check for the model was included in Supporting Information

269 Text S2.

### 270 2.3 Bedform migration

271 In this study, ripples formation was qualitatively determined using the bedform stability  
272 diagram (Figure 3). This diagram is a summarized reference for examining equilibrium bed  
273 configurations in unidirectional flow, derived from a series of flume experiments and field  
274 studies (Ashley, 1990). Besides, a series of quantitative criteria (Text S1 in the supporting  
275 information: Criteria for ripple migration) was examined to ensure ripple formation under the  
276 modeled scenarios and the achievement of dynamic equilibrium. For a specific grain size of  
277 streambed sediment ( $D_{50}$ ), particular stream velocities ( $U$ ) satisfying all these criteria are  
278 selected and displayed in Figure 3. All simulation scenarios were listed in the Table S1.



279  
280 **Figure 3.** The bedform stability diagram (modified from Ashley, 1990) showing the bedform  
281 properties and hydraulic conditions considered in this study. Different colors indicate different  
282 median grain sizes of the streambed sediments. For each sediment grain-size scenario, various

283 streamflow conditions were simulated, corresponding to the velocity values shown on the y-axis

284 Ripple migration velocities were implemented using an empirical relation after Coleman

285 and Melville (1994), which was derived from flume experiments:

$$286 \quad \frac{u_c}{(u^* - u_{cr}^*)(\tau^* - \tau_{cr}^*)} (H_d / D_{50} - 3.5)^{1.3} = 40 \quad (15)$$

287 where  $u^* = (gHS)^{0.5}$  [L T<sup>-1</sup>] is the bed shear velocity,  $S$  [-] is the stream gradient and calculated

288 by Chezy equation ( $U = H^{2/3} S^{1/2} / n$ , where  $n$  [-] is the Manning coefficient and assumed to be

289 0.02 for sand).  $u_{cr}^*$  [L T<sup>-1</sup>] is the critical bed shear velocity and it can be calculated by the critical

290 Shield parameter  $\tau_{cr}^*$  ( $\tau_{cr}^* = \tau_{cr} / g(\rho_s - \rho)D_{50}$ ,  $u_{cr}^* = (\tau_{cr} / \rho)^{0.5}$ ,  $\rho_s$  [M L<sup>-3</sup>] and  $\rho$  [M L<sup>-3</sup>] are the

291 density of sediment and water), and  $\tau^*$  is the shield number related to the bed shear velocity ( $\tau^* =$

292  $u^{*2} / rgD_{50}$ ;  $r$  [-] is the submerged specific gravity of sediment =  $(\rho_s - \rho) / \rho$ ). The critical shields

293 parameter  $\tau_{cr}^*$  defines the threshold for the initialization of motion, and it is determined by the

294 dimensionless particle parameter  $D^*$  [-] (Soulsby, 1997; Zheng et al., 2019):

$$295 \quad \tau_{cr}^* = \frac{0.3}{1 + 1.2D^*} + 0.055 [1 - \exp(-0.02D^*)] \quad (16)$$

296 where  $D^* = D_{50} \cdot (rg/v^2)^{1/3}$ ,  $v$  is the kinematic viscosity of water [L<sup>2</sup> T<sup>-1</sup>]; The derived celerity was

297 substituted into Equation (10) to determine the migration of sinusoidal pressure head profile

298 with ripples moving.

## 299 **2.4 Governing non-dimensional numbers**

300 The characteristics of the modeled system were depicted by a series of non-dimensional

301 numbers, which represent the relative dominance of various forces, transport, and reaction

302 processes in this system. Firstly, the Reynolds number  $Re$  was used to characterize the flow

303 condition of surface water (Cardenas and Wilson, 2006):

$$304 \quad Re = \frac{UH_d}{\nu} \quad (17)$$

305 where  $\nu$  [ $L^2 T^{-1}$ ] represents kinematic viscosity of water.

306 The dimensionless parameter  $U_r$  [-] was introduced to represent the relative magnitude of  
307 bedform celerity and the pressure-induced pore water velocity driven by pressure variation over  
308 the ripple surface and upwelling groundwater:

$$309 \quad U_r = \frac{\theta \cdot u_c - u_s}{u_p} \quad (18)$$

310 where  $u_s$  [ $L T^{-1}$ ] is the seepage velocity of the underflow induced by stream gradient ( $u_s = KS$ ),

311 and thus the characteristic horizontal velocity is  $u_c - u_s/\theta$ .  $u_p/\theta$  [ $L T^{-1}$ ] is the pore water velocity

312 induced by pumping process and is calculated using the analytical solution after Boano et al.

313 (2009) and Fox et al. (2014) accounting for vertical groundwater flux ( $u_q$  [ $L T^{-1}$ ]):

$$314 \quad u_p = u_{p,0} \sqrt{1 - (u_q / \pi u_{p,0})^2} + (|u_q| / \pi) \sin^{-1} (|u_q| / \pi u_{p,0}) - (|u_q| / 2) \quad (19)$$

$$315 \quad u_{p,0} = a \frac{KU^2}{g\lambda} \left( \frac{H_d/H}{0.34} \right)^m \quad (20)$$

316 where  $u_{p,0}$  [ $L T^{-1}$ ] represents the hyporheic exchange solely driven by pressure variation over the

317 sediment-water interface; if  $U_r > 1$ , turnover process dominates and controls the hyporheic

318 exchange, otherwise, the system is pumping process dominated (Jiang et al., 2022).

319 The relative magnitude of hyporheic exchange flux driven by pressure variation along the

320 riverbed surface and upwelling groundwater flux was determined as:

321 
$$U_b = \frac{u_q}{u_{p,0}} \quad (21)$$

322 The relative dominance of hyporheic exchange and biogeochemical reaction in nitrate  
 323 removal can be defined by the Damköhler number (Ocampo et al., 2006; Zarnetske et al., 2012;  
 324 Zheng et al., 2019):

325 
$$Da = \frac{\tau_T}{\tau_R} \quad (22)$$

326 the characteristic timescale for the transport of solutes through the ripple was estimated as  
 327 (Azizian et al., 2015):

328 
$$\tau_T = \frac{\lambda\theta}{\pi^2 u_p} \quad (23)$$

329 and the reaction timescale ( $\tau_R$ ) represents the time needed to consume dissolved oxygen of  
 330 hyporheic water to a prescribed anoxic environment threshold (2 mg/L). The reaction timescale  
 331 was described as:

332 
$$\tau_R = \frac{\ln(c_{O_2}/c_{O_2,\text{lim}})}{V_{AR}} \quad (24)$$

333 biogeochemical reactions are transport-limited when  $Da < 1$ . The biogeochemical reactions  
 334 depended on reaction kinetics due to the brevity of the time that reactants spend within the HZ.  
 335 Under these low  $Da$  conditions, the HZ remains oxic conditions, resulting in a minimal or no  
 336 denitrification to occur. Conversely, when  $Da > 1$ , the residence time of reactants exceeds the  
 337 reaction time, and thus oxygen is consumed and favors for the occurrence of denitrification in  
 338 anoxic conditions (Jiang et al., 2022; Zarnetske et al., 2011a).

## 339 2.5 Model setup and parametrization

340 All parameter values in this study were shown in Table 1. The bedform geometry of Ping et  
341 al. (2022) was adopted for this study (the ripples located at  $\lambda_c = 0.15$  m with a height of  $H_d =$   
342 0.02 m). Here grain sizes  $D_{50}$  of 0.08, 0.15, 0.22 and 0.36 mm were considered, typically falling  
343 within characteristic grain diameters on sandy riverbeds (Ahmerkamp et al., 2017; Harvey et al.,  
344 2012). The permeability of riverbed was calculated using the empirical relation  $k =$   
345  $Da' \times 735 \times 10^6 \times D_{50}^2$  (where  $Da' = 9.869 \times 10^{-13}$  is the conversion factor for unit Darcy to  $m^2$ ;  
346 Gangi, 1985).

347 The concentrations of DOC,  $O_2$ , and  $s\text{-NO}_3^-$  in stream were specified as 30 mg/L, 8 mg/L,  
348 and 5 mg/L. This configuration represents a pristine stream characterized by moderate nutrient  
349 levels (Ocampo et al., 2006). The  $g\text{-NO}_3^-$  in groundwater was set as 15 mg/L, representing the  
350 chemical signature of nitrate-contaminated groundwater that lacks both oxygen and organic  
351 matter (Hester et al., 2014). The maximum reaction rate and corresponding functional microbial  
352 concentration for AR and DN were listed in Table 1, the choose biogeochemical values are  
353 consistent with the parameter setting of nutrient cycling in hyporheic zones and riparian zones  
354 (Gu et al., 2008; Nogueira et al., 2021; Zarnetske et al., 2012).

355 **Table 1.** Model parameters used in numerical simulations

Parameter	Description	Value
$l$ [m]	Streambed depth	0.16 <sup>a, b</sup>
$l_c$ [m]	Ripple crest	0.15 <sup>a, b</sup>
$\lambda$ [m]	Wavelength of ripple	0.2 <sup>a, b</sup>

$H_d$ [m]	Height of ripple	0.02 <sup>a, b</sup>
$H$ [m]	Stream water depth	0.1 <sup>a, b</sup>
$\theta$ [1]	Porosity	0.38 <sup>e</sup>
$\alpha_L$ [m]	Longitudinal dispersivity	0.01 <sup>f</sup>
$\alpha_T$ [m]	Transverse dispersivity	0.001 <sup>f</sup>
$K_{inh}$ [mg L <sup>-1</sup> ]	Inhibition constant	0.25 <sup>c, d</sup>
$K_{DOC}$ [mg L <sup>-1</sup> ]	Half-saturation constant for dissolved organic carbon	6 <sup>c, d</sup>
$K_{NO_3}$ [mg L <sup>-1</sup> ]	Half-saturation constant for nitrate	1 <sup>c, d</sup>
$K_{O_2}$ [mg L <sup>-1</sup> ]	Half-saturation constant for dissolved oxygen	0.5
$V_{DN}$ [h <sup>-1</sup> ]	Maximum specific uptake rate for denitrification	1 <sup>c, d</sup>
$V_{AR}$ [h <sup>-1</sup> ]	Maximum specific uptake rate for aerobic respiration	2 <sup>c, d</sup>
$C_{DOC}$ [mg L <sup>-1</sup> ]	Concentration of dissolved organic carbon in stream	30
$C_{O_2}$ [mg L <sup>-1</sup> ]	Concentration of dissolved oxygen in stream	8
$C_{s-NO_3^-}$ [mg L <sup>-1</sup> ]	Concentration of nitrate in stream	5
$C_{g-NO_3^-}$ [mg L <sup>-1</sup> ]	Concentration of nitrate in groundwater	15

356 <sup>a</sup> Janssen et al. (2012) <sup>b</sup> Ping et al. (2022) <sup>c</sup> Zarnetske et al. (2012) <sup>d</sup> Sawyer (2015) <sup>e</sup> Ahmerkamp et al.

357 (2015) <sup>f</sup> Bardini et al. (2012)

358 The following distinct model experiments were carried out: The Reynolds number, i.e.,  
359 mean stream velocity, was varied for  $Re = 2000$ – $6000$  in intervals of 500, with corresponding  
360 stream water velocities of  $U = 0.1$ – $0.3$  m/s. The range of  $U_b$  was set from 0.3 to 0.7 in intervals  
361 of 0.1; correspondingly, the upwelling groundwater flux  $u_q$  was ranged between  $0.3 \times u_{p,0}$  and  
362  $0.7 \times u_{p,0}$ . A larger upward flux than  $0.9 \times u_{p,0}$  would eliminate the entire hyporheic flow cell, thus

363 the maximum boundary flux was set at a value slightly below this threshold. Meanwhile a  
364 minimum of  $0.2 \times u_{p,0}$  ensures that upwelling groundwater is still mixing with surface water with  
365 minor influences on hyporheic flow cell. Longitudinal and transverse dispersivities ( $\alpha_L$  and  $\alpha_T$ )  
366 are important values for obtaining accurate mixing. Here sensitivity analysis of local dispersion  
367 was conducted by varying  $\alpha_L$  from 0.001 to 0.015 m, with  $\alpha_T$  set to 1/10 of  $\alpha_L$ . Molecular  
368 diffusion was fixed at  $10^{-9}$  m<sup>2</sup>/s, which has a secondary effect on solute dispersion process. This  
369 sensitivity analysis is provided in the Supporting Information (Text S4).

370 The finite element software, COMSOL Multiphysics (version 6.1) was used to solve the  
371 Darcy flow and multi-component solute transport model. Three computational grids were  
372 evaluated to ensure grid resolution independence of simulated results, confirming that the grid is  
373 sufficiently refined to capture mixing dynamics and minimize numerical dispersion. The fine,  
374 base and coarse grid sizes were 1.5 mm, 2 mm, and 2.5 mm, respectively. The grid  
375 independence analysis was provided in the Supporting Information (Text S2). For the  
376 simulations, the base grid size was selected, with the domain discretized into 19,940 cells. To  
377 maintain a constant bedform displacement ( $\Delta x$ ) per timestep, the simulation was conducted with  
378  $\Delta x = 2$  mm, while  $dt$  was adjusted in inverse proportion to the migration celerity  $u_c$ . The total  
379 duration of the simulation was set to be equal to the time needed for hundreds of ripples to travel  
380 across the modeled domain until the hyporheic exchange and biogeochemical processes reached  
381 quasi-steady states.

## 382 **2.6 Model Metrics**

### 383 2.6.1 Mixing of surface water and groundwater

384 Here, macroscopic mixing is defined as the collocation of surface water (SW) and  
385 groundwater (GW) within a specific aquifer volume (e.g., a numerical model element or cell), a  
386 process that causes solutes to be present simultaneously in an overlapping region (Nogueira et  
387 al., 2022). There is no established standard for the threshold governing SW and GW fractions  
388 during the mixing process; nonetheless, the general recognition is that mixing occurs when the  
389 GW proportion falls within the range of 10% to 90% (Hester et al., 2013; Woessner et al., 2000).  
390 This interval effectively distinguishes the occurrence of mixing, where SW and GW interact  
391 dynamically, from the two endmembers: pure GW (>90%) and pure SW (<10%). To evaluate  
392 the influence of threshold variations on mixing metrics, sensitivity analysis was conducted to  
393 examine three alternative GW fraction ranges: 10%–90% (wider interval), 16%–84%, and 20%–  
394 80% (narrower range). Thus, mixing flux and mixing zone were calculated based on these three  
395 thresholds.

396 A constant concentration boundary condition of conservative tracer ( $c_{gw} = 1 \text{ mg/L}$ ) in GW  
397 was specified to represent the tracer signature of groundwater, following the methods outlined  
398 by Hester et al. (2013, 2014). The groundwater-borne tracer that undergoes mixing as it  
399 transitions from flow paths originating at the bottom boundary to those emerging at the  
400 streambed surface was quantified to determine the net effect of mixing. The streambed surface  
401 was divided into three zones (Figure 1): “SW IN”, where surface water enters the riverbed layer;  
402 “SW OUT”, where surface water discharges back into the overlying water column; and “GW  
403 OUT”, where upwelling groundwater discharges into the stream. The conservation tracer flux

404 for the SW OUT zone was used to describe mixing. If no mixing occurred, all the conservative  
405 tracer entering the model at the bottom boundary would exit through the GW OUT zone on the  
406 riverbed surface. The arrival of conservative solute at the riverbed surface is defined as the start  
407 of mixing, and the complete leave of all the conservation solute from the riverbed is defined as  
408 the end of mixing. Due to dispersion, the groundwater-borne tracer gradually spreads through  
409 the streambed and eventually crosses the sediment-water interface. The terms “mixing start and  
410 end” denote the period over which mixing is calculated.

411 The mixing flux across the riverbed surface was determined by integrating the outward  
412 volumetric flux containing groundwater-borne conservation solute within the specified  
413 concentration range (i.e.,  $c_{gw} = 0.1\text{--}0.9$  mg/L,  $c_{gw} = 0.16\text{--}0.84$  mg/L,  $c_{gw} = 0.2\text{--}0.8$  mg/L). This  
414 flux corresponds to groundwater flowing through “SW OUT” zone. Concurrently, the mixing  
415 zone was calculated by integrating the riverbed area that contains groundwater-borne  
416 conservation solute within the specified concentration range. The average mixing flux and  
417 mixing zone over the whole mixing period were computed and termed the mixing flux (*MF*) and  
418 mixing zone, respectively. The mixing fraction (*Fmix*) was computed as the ratio of the mixing  
419 flux to the total hyporheic flux, which was derived from integrating the volumetric flux along  
420 the sediment-water interface (including both SW OUT and GW OUT). *Fmix* serves as a metric  
421 to quantify the proportion accounted for by the SW-GW mixing flux within the overall flux of  
422 SW and GW interaction across the sediment-water interface. *Amix* is defined as the ratio of the  
423 mixing zone to the entire modeled domain, representing the proportion of the riverbed occupied  
424 by the mixing zone.

425 2.6.2 Nitrate reaction rate and efficiency

426 When the hydro-physical and biogeochemical conditions reach a quasi-steady state, the  
 427 average flux of stream- or groundwater- borne nitrate entering the riverbed layer over the final  
 428 serval periods of ripple migration was calculated:

$$429 \quad M_{in,s-NO_3^-} = \frac{1}{w} \sum_T B \int v c_{s-NO_3^-} - \theta D_{ij} \cdot \nabla c_{s-NO_3^-} dL_{top} \quad (25)$$

$$430 \quad M_{in,g-NO_3^-} = \frac{1}{w} \sum_T B \int v c_{g-NO_3^-} - \theta D_{ij} \cdot \nabla c_{g-NO_3^-} dL_{bottom} \quad (26)$$

431 where  $B$  [L] is the per unit width,  $\theta$  [-] is the sediment porosity, and  $w = T/dt$  [-];  $L_{top}$  and  $L_{bottom}$   
 432 refer to the top boundary BC and bottom boundary AD, respectively.

433 The total amount of nitrate removed by NMD denitrification and MD denitrification were  
 434 calculated as follows during the same time interval:

$$435 \quad M_{NMD} = \frac{1}{w} \sum_T B \int R_{DN}(c_{s-NO_3^-}) dA \quad (27)$$

$$436 \quad M_{MD} = \frac{1}{w} \sum_T B \int R_{DN}(c_{g-NO_3^-}) dA \quad (28)$$

437 where  $A$  [L<sup>2</sup>] is the area of the streambed.

438 Nitrate removal efficiency was quantified as the rate of nitrate removed from the riverbed  
 439 layer divided by the nitrate flux entering the riverbed layer:

$$440 \quad N_{RE-NMD} = \frac{M_{NMD}}{M_{in,s-NO_3^-}}, \quad N_{RE-MD} = \frac{M_{MD}}{M_{in,g-NO_3^-}} \quad (29)$$

## 441 **3. Results**

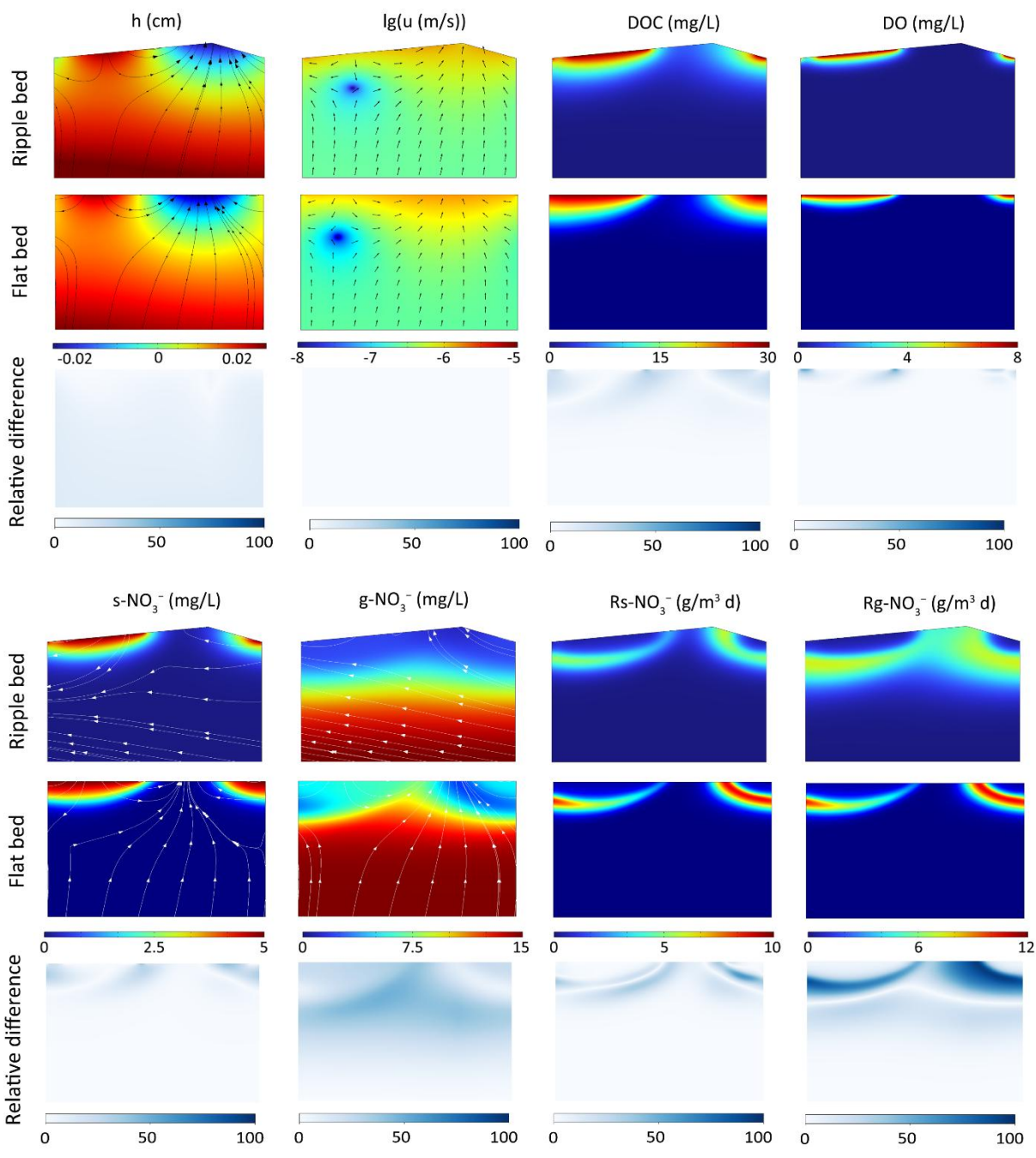
### 442 **3.1 Model validation**

#### 443 3.1.1 Validation of flat bed model with triangular ripple model

444 Model validation was conducted in two steps, with two numerical methods employed to  
445 represent moving bedforms. Beyond simulating porewater flow and reactive solute transport in a  
446 fixed frame of reference with a flat riverbed surface, a reference frame moving with triangular  
447 ripples was also adopted to capture bedform migration, following the methods of Bottacin-  
448 Busolin and Marion (2010), Ahmerkamp et al. (2015), and Kessler et al. (2015). The latter  
449 method captures bedform migration while preserving the ripple shape, and comparisons between  
450 the two approaches were conducted to examine the impact of neglecting ripple geometry on the  
451 simulated results.

452 A typical case ( $Re = 3000$ ,  $U_b = 0.6$  and  $D_{50} = 0.15$  mm) was chosen here for comparison.  
453 The relative differences between these two modeling approaches were compared after  
454 normalizing the triangular ripple shape to a flat riverbed by projecting the values on the sloped  
455 edges onto the horizontal straight boundary. The overall patterns of pressure head, Darcy  
456 velocity, and stream-borne solute plume distributions were mostly similar (Figure 4). The  
457 difference in groundwater-borne nitrate plumes is attributed to the distinct advection velocities  
458 for reactive solute transport. Specifically, the moving reference frame involves a transformation  
459 of the horizontal coordinate system, based on the assumption that the frame of reference moves  
460 in the direction of bedform migration and at the same migration celerity; in this frame, the  
461 modeled advection velocity of reactive solutes is the seepage velocity minus the celerity. Thus,

462 in the triangular ripple model,  $g\text{-NO}_3^-$  flows upstream with larger advection velocities, resulting  
 463 in a more uniform solute plume; in contrast, it exits the riverbed across the entire riverbed  
 464 surface in the flat bed model (see the white streamlines). Correspondingly, discrepancies emerge  
 465 in the crest area of the MD denitrification zone.



466  
 467 **Figure 4.** Comparison of hyporheic flow and reactive solute transport modeling results from the

468 flat bed model and the triangular ripple model. Streamlines and arrows in the Darcy flow field  
469 indicate porewater flow, while streamlines in nitrate solute plumes represent the advection  
470 velocity of reactive solute transport.

471 Compared with the triangular ripple model, the flat bed model exhibits larger hyporheic  
472 exchange flux, mixing flux, and stream-borne nitrate influx. The relative difference are  
473 approximately 5%. Meanwhile, both the total MD and NMD denitrification rates are higher in  
474 the triangular ripple model than in the flat bed model, with relative difference around 10%.  
475 Additionally, the spatial relative differences between these two models are depicted in Figure 4.  
476 The relative difference is the absolute difference between the values calculated by the two  
477 models at the same coordinate location divided by the maximum value in the flat bed model.  
478 Note that the largest differences occur in the MD denitrification hotspots. Spatially, the flat bed  
479 model captures the hotspots of the denitrifying zone but underestimates the rates, potentially  
480 leading to an underestimation of groundwater borne nitrate removal efficiency. To further assess  
481 the differences between the two models and their reliability, two methods were utilized to  
482 perform validation against the experiments by Wolke et al. (2020).

### 483 3.1.2 Validation of numerical models with laboratory experiments

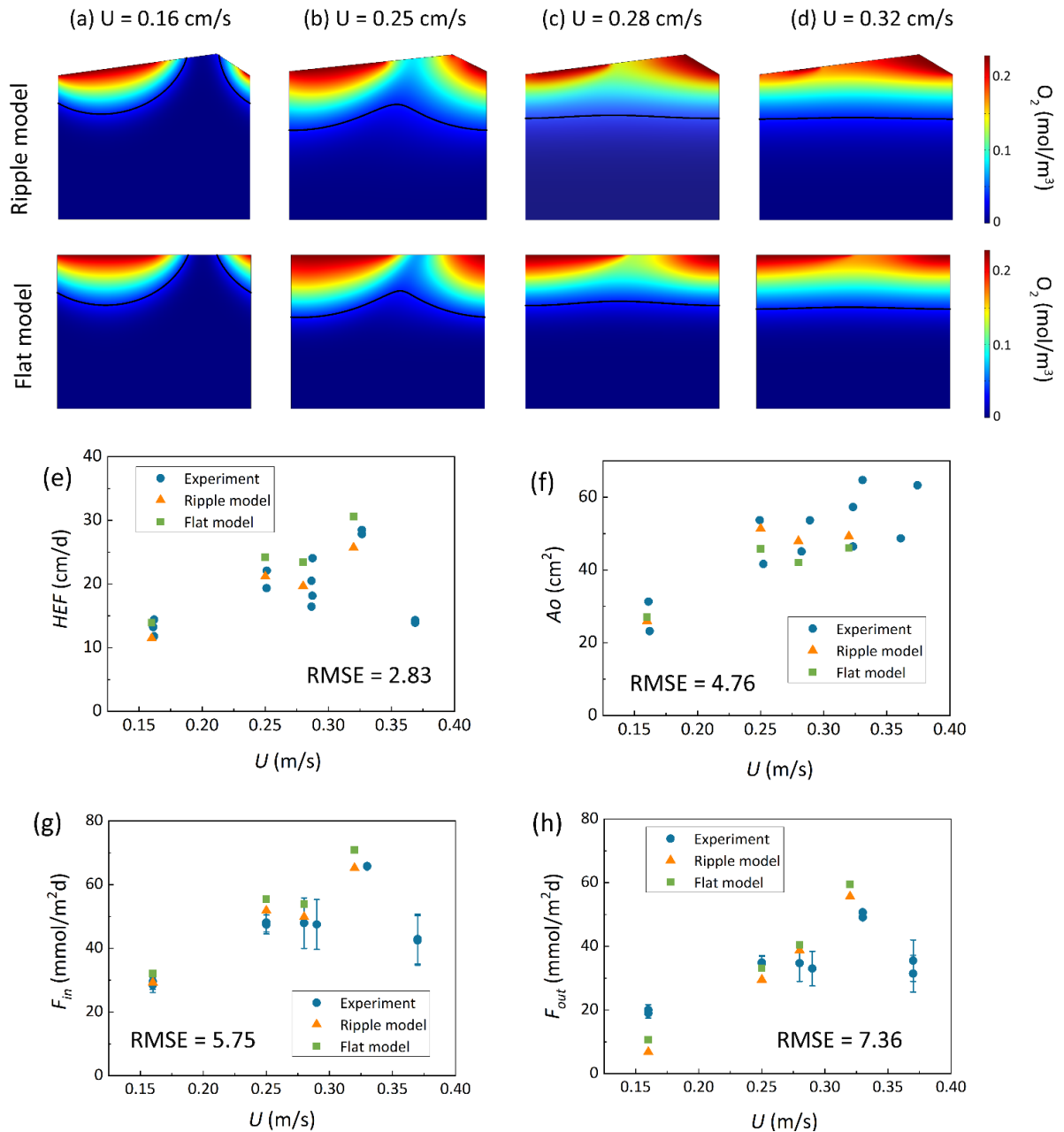
484 The developed models were validated through comparison with Wolke et al.'s (2020) flume  
485 experiments, which investigated the evolution of oxygen in the riverbed under varying  
486 conditions of mean stream velocity (0.16–0.32 m/s) and bedform migration celerity (0–0.394  
487 cm/h). The experiment was designed with a total of 5 operating conditions, each of which was  
488 repeated twice and labeled as Set 1 and Set 2. Oxygen distribution within sediments was  
489 measured via planar optodes, and the oxygenated zone was defined as regions where oxygen

490 saturation exceeds 15%. Oxygen consumption was observed within riverbed layer and aerobic  
491 respiration is widely recognized as the dominant process driving oxygen consumption within  
492 riverbed sediments (Ahmerkamp et al., 2017; Reeder et al., 2018). In their experiments, a fixed  
493 amount of NaCl was added to surface water; this NaCl was then used to compute hyporheic  
494 exchange flux ( $HEF$ ) from the decline in its concentration, following the empirical equation by  
495 Fox et al. (2018). The oxygen influx ( $F_{in}$ ) and outflux ( $F_{out}$ ) were calculated by multiplying  $HEF$   
496 by the surface water oxygen concentration and the mean oxygen concentration in the  
497 oxygenated zone, respectively.

498 Two numerical models: the flat bed model and the triangular ripple model, were developed  
499 under the same hydraulic conditions, with their parameters adjusted to fit  $HEF$ ,  $F_{in}$ ,  $F_{out}$ , and  $Ao$   
500 to experimental data. The model parameters were summarized in Supporting Information Text  
501 S3: Model validation. All physical and hydraulic parameters (e.g., ripple geometry, streamflow,  
502 bedform migration velocity, porosity, and permeability) were used exactly as reported in Wolke  
503 et al. (2020) experiments without any adjustment. Only the biogeochemical reaction parameters  
504 (e.g., maximum oxygen consumption rate, and half-saturation constant for oxygen) were  
505 calibrated to match the observed oxygen plume, as these parameters are difficult to measure  
506 directly in dynamic streambed environments and are commonly calibrated in reactive transport  
507 models.

508 In the numerical model,  $HEF$  was calculated by integrating the volumetric flux over the  
509 inflow zones along the sediment-water interface. Oxygen transport was governed by the  
510 advection-dispersion-reaction equation, where oxygen consumption occurred through aerobic  
511 respiration following the Monod kinetics described by Equation (8). The  $F_{in}$  and  $F_{out}$  were then

512 computed by multiplying the *HEF* by the oxygen concentration in the surface water and the  
513 oxygen concentration over the outflow zones along the riverbed surface, respectively. The  
514 oxygenated area was calculated by integrating the riverbed portions where oxygen saturation  
515 exceeds 15%. Based on the criteria for ripple migration, it was determined that under the  
516 hydraulic conditions of Run 5, ripples could not migrate while maintaining their shapes due to  
517 increased stream flow velocity. Therefore, the model validation simulations considered four  
518 hydraulic conditions of Run 1 to 4.



519

520 **Figure 5.** Comparison of numerical modeled oxygen distribution, (e) hyporheic exchange flux,  
 521 (f) summed oxic zone and (g) oxygen influx and (h) oxygen outflux and experimental  
 522 measurements by Wolke et al. (2020) under various conditions. The units of RMSE are (e) cm/d,  
 523 (f) cm<sup>2</sup>, (g) mmol/m<sup>2</sup>d, and (h) mmol/m<sup>2</sup>d.

524 For stationary and slow-migrating beds, the spatial distribution of oxygen creates a  
 525 conchoidally shaped plume beneath the bedform; in contrast, beneath fast-migrating beds, the  
 526 oxygen plume shifts to a more uniform front. The  $HEF$ ,  $F_{in}$ ,  $F_{out}$ , and  $A_o$  simulated using both

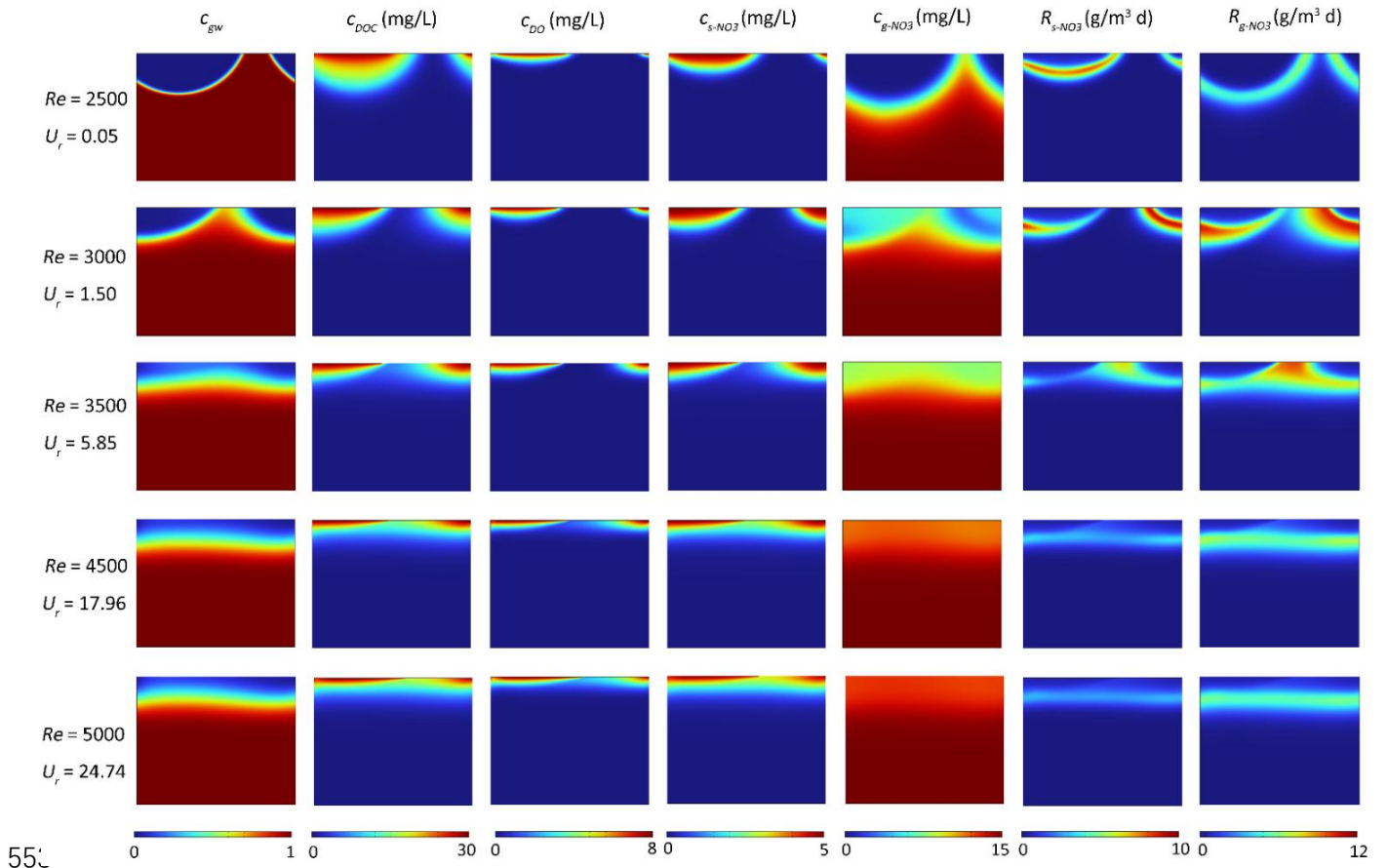
527 the ripple bedform model and the flat bed model were presented in Figure 5; these results are in  
528 good qualitative and quantitative agreement with the measurements of Wolke et al. (2020). The  
529 root means square error (RMSE) between the experimentally measured values and those  
530 simulated by the flat bed model were further calculated. All RMSE values fall within reasonable  
531 ranges, indicating the critical processes of bedform migration and oxygen dynamic are captured  
532 by the numerical models.

### 533 **3.2 Effect of bedform migration on mixing and solute dynamic**

534 To simulate the range of natural environmental conditions, the reactive transport equations  
535 were solved for different stream velocities, grain sizes and groundwater upwelling fluxes, which  
536 include a corresponding range of ripple migration celerities and sediment permeabilities derived  
537 from the empirical relations. As an example, the patterns of pore water transport as well as SW  
538 and GW mixing are shown for a grain size of 0.15 mm, a constant ratio between pumping driven  
539 hyporheic exchange flux and upwelling GW flux  $U_b = 0.6$ , and four different stream velocities,  
540 that is four different  $Re$  numbers.

541 For low surface water flow velocity ( $Re = 2500$ ), no migration of bedform is predicted by  
542 the model. SW enters the riverbed layer in the high-pressure region on the stoss side, flows  
543 through the porous medium, and exits the riverbed layer in the low-pressure region on the lee  
544 side, forming a typical conchoidally shaped hyporheic flow cell. Upwelling GW is diverted  
545 around the hyporheic flow cell, mixes with SW, and then exits into the overlying water from  
546 both sides, in patterns similar to those shown previously by Fox et al. (2014) and Hester et al.,  
547 (2019). SW and GW mixing zone (i.e. the mixing area where the fraction of GW ranges between  
548 16% and 84%) emerges as a thin band along the hyporheic flow cell, and covers over 2.97% of

549 the modeled domain. Meanwhile, NMD denitrification occurs below the oxygen plume with the  
 550 reactive zone in a conchoidal shaped distribution, while MD denitrification reactive zone  
 551 develops along the edge of the mixing zone, where DOC from SW meets nitrate from GW (row  
 552 1 in Figure 6).



554 **Figure 6.** Effect of bedform migration on riverbed biogeochemistry for  $U_b = 0.6$  and  $D_{50} = 0.15$   
 555 mm. Shown are profiles of (column 1) conservation solute representing groundwater fraction  
 556 ( $c_{gw}$ ), (column 2) DOC concentration ( $c_{DOC}$ ), (column 3)  $O_2$  concentration ( $c_{DO}$ ), (column 4) s-  
 557  $NO_3^-$  concentration ( $c_{s-NO_3^-}$ ), (column 5) g- $NO_3^-$  concentration ( $c_{g-NO_3^-}$ ), (column 6) non-  
 558 mixing-dependent (NMD) denitrification rate ( $R_{s-NO_3^-}$ ) and (column 7) mixing-dependent (MD)  
 559 denitrification rate ( $R_{g-NO_3^-}$ ).

560 At a surface water  $Re$  of 3000, bedforms migrate at a low celerity of 1.04 cm/h. This low  
561 migration rate has minimal impact on the plumes of stream-borne  $O_2$  and  $s\text{-NO}_3^-$ . The outflow  
562 zone of groundwater-borne solutes ( $c_{gw}$  and  $g\text{-NO}_3^-$ ) exhibits a slight upstream shift,  
563 approaching the middle of the riverbed surface. The size of SW and GW mixing zone (GW  
564 faction: 16%–84%) increases to 10.06% of the modeled domain. Furthermore, both the NMD  
565 and MD denitrifying rates are enhanced at the start of bedform migration (row 2 in Figure 6).

566 With increasing stream velocity ( $Re = 3500$ ), bedform migration drives continuous changes  
567 in pressure distribution. The simulated hyporheic flow cells move downstream and decrease in  
568 size at the same time. The shape of the SW and GW mixing zone changes distinctly, forming a  
569 horizontal band with a wider range 10.71% of the whole domain (GW faction: 16%–84%). The  
570 penetration of stream-derived solutes into the streambed is reduced, with a more gradual  
571 concentration gradient in the horizontal and vertical directions, whereas the  $g\text{-NO}_3^-$  plume is  
572 uniformly distributed horizontally. Both NMD and MD denitrification hot spots form in the  
573 central position near the sediment-water interface as the bedform moving (row 3 in Figure 6).

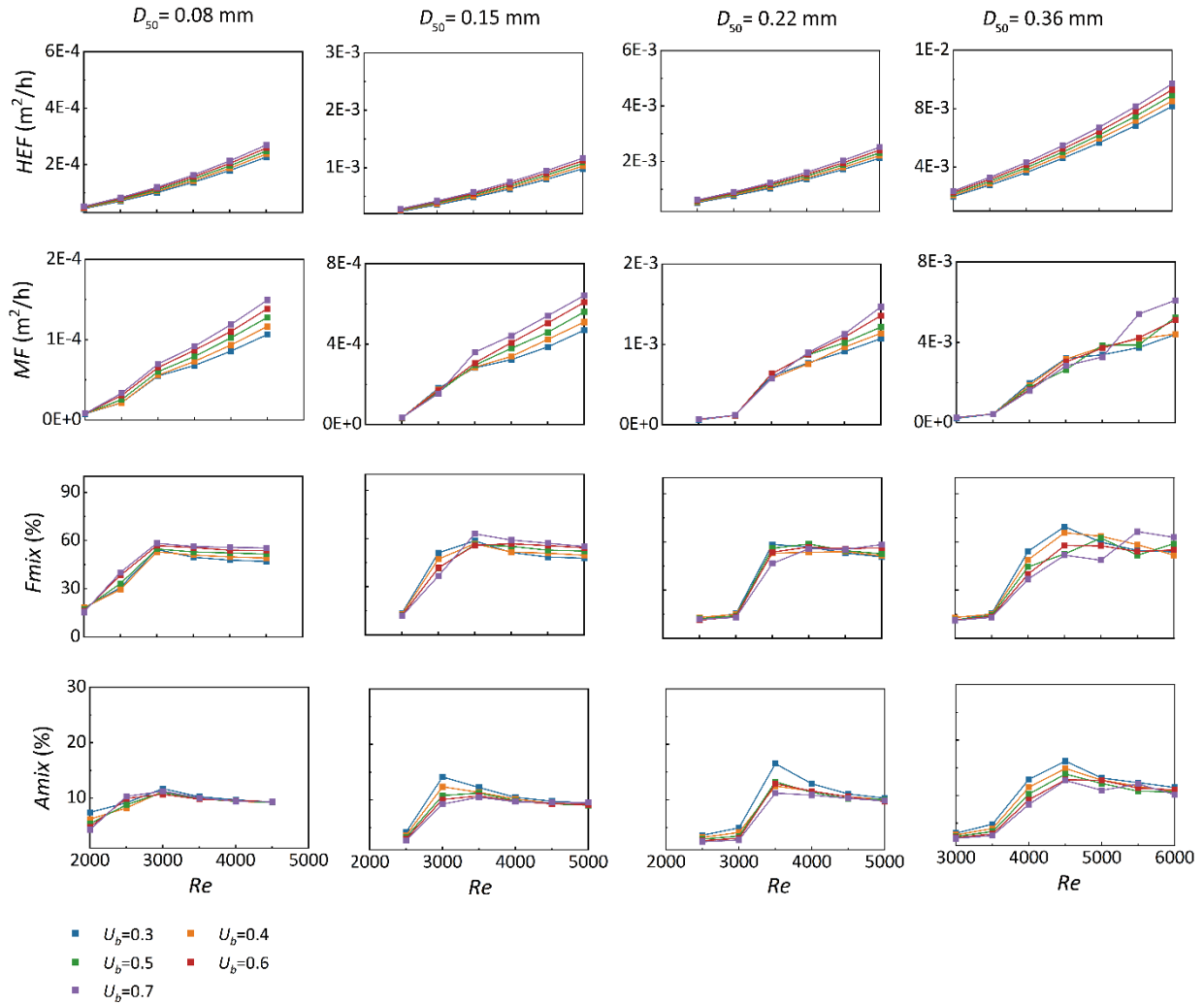
574 When bedform migration is further increased ( $Re = 4500$  and  $5000$ ), bedform migration  
575 fully dominates over the pore water flow, and hence, continuous solute layers are found in the  
576 subsurface (as depicted in row 4 and 5 of Figure 6). The penetration depths of stream-borne  
577 solutes are decreased in comparison to those in slow- to medium- fast migrating bedforms. The  
578 NMD and MD denitrification zones become thin and move upward with decreased reaction  
579 rates. Similar to the conclusions obtained in previous studies (Kessler et al., 2015; Zheng et al.,  
580 2019), bedform migration reduces the penetration depth of solute and the scope of hyporheic  
581 exchange cell. We also found that bedform migration increases the size of mixing zone between

582 surface water and groundwater. The SW and GW mixing zone accounts for 9.30% and 9.14% of  
583 the domain area, respectively (take the GW fraction 16%–84% for example).

### 584 **3.3 Effect of migration celerity on mixing regimes**

585 The mixing intensity across the riverbed surface and the size of the mixing area within the  
586 subsurface were estimated by simulating four different grain sizes and five upwelling GW  
587 fluxes, under varying stream velocities associated with the corresponding bedform celerity. The  
588 evolutions of the hyporheic exchange flux, net mixing flux and size of mixing zone with  
589 increasing  $Re$  number were summarized in Figure 7. The 16–84% GW fraction range was  
590 displayed here to evaluate how migration celerity affects mixing regimes.

591 As shown in Figure 7, across various grain sizes, both  $HEF$  and  $MF$  increase with  
592 increasing stream velocity and bedform celerity. Nevertheless, the mixing fraction exhibits a  
593 significant increase at the onset of bedform migration, with a tendency to stabilize or decrease  
594 moderately as celerity further increases. This phenomenon is attributed to enhanced mixing  
595 between SW and discharging GW along the entire horizontal riverbed in moving bedforms—  
596 contrasting with stationary bedforms, where mixing occurs solely along the typical crescent-  
597 shaped hyporheic exchange flow cells (Figure 6). Additionally, when bedforms start moving and  
598 move at moderate velocities, the SW-GW mixing zone shows a significant increase compared to  
599 stationary ones. As bedform migration celerity accelerates, the extent of the mixing zone  
600 gradually approaches a plateau, with slight reductions observed at higher celerities.



601  
 602 **Figure 7.** The variation of hyporheic exchange flux ( $HEF$ , row 1) and mixing flux ( $MF$ , row 2)  
 603 across the sediment-water interface, the proportion of mixing flux to hyporheic exchange flux  
 604 ( $Fmix$ , row 3) and the ratio of mixing zone to whole domain ( $Amix$ , row 4) with stream velocity  
 605 and associated bedform celerity across different medium grain size when  $U_b = 0.3-0.7$ .

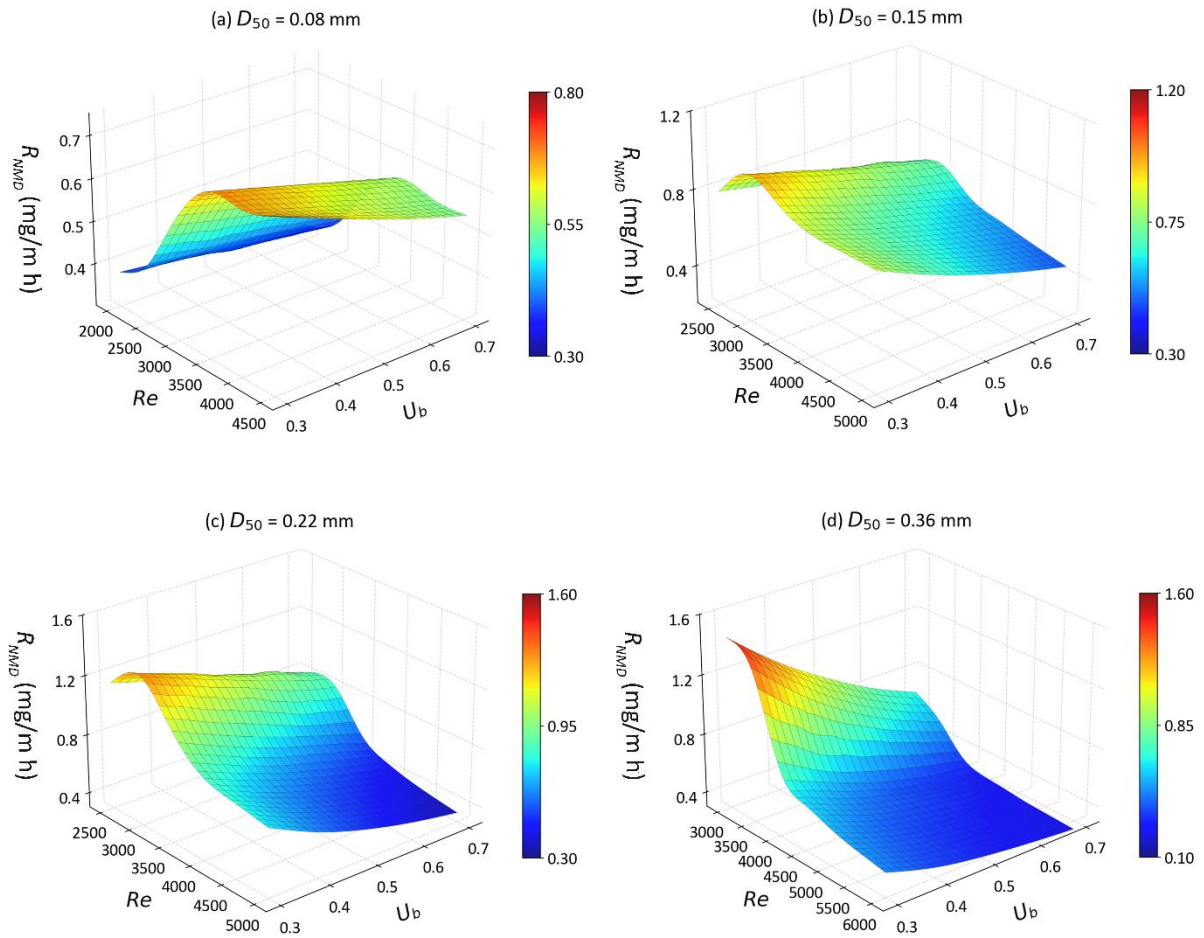
606 Although the GW fraction range determines both mixing flux and scope, it does not alter  
 607 the effect of migration celerity on these mixing patterns. A broader groundwater fraction range  
 608 induces a larger mixing flux, an increased  $Fmix$ , and a wider mixing zone; nonetheless,  $Amix$   
 609 persists as a relatively small scope (about 10–15% of the full domain) within the riverbed.  
 610 Relatively moderate differences in computed  $MF$  and  $Fmix$  are observed between the narrower

611 range (20–80%) and the baseline range (16–84%). For bedforms of different sediment grain  
612 sizes,  $MF$  represents around 60% of the total  $HEF$  when bedforms are moderately to fast-  
613 moving, compared with approximately 20% when they are stationary or slow-moving.

614 Taking a grain size of 0.15 mm and a constant ratio between pumping-driven hyporheic  
615 exchange flux and upwelling groundwater flux ( $U_b = 0.6$ ) as an example, we varied  $\alpha_L$  from  
616 0.001 to 0.015 m (Figure S5). While increased longitudinal and transverse dispersivities clearly  
617 enhance  $F_{mix}$  and  $A_{mix}$ , they do not modify the influence of bedform migration on these mixing  
618 metrics. This confirms that greater dispersivity enhances SW and GW mixing, leading to a  
619 larger proportion of hyporheic exchange flux involved in mixing and an expanded mixing zone.  
620 As such, reliable dispersion parameter estimates are essential for accurate mixing magnitude  
621 assessments. Additionally,  $F_{mix}$  and  $A_{mix}$  values obtained under various GW fraction ranges  
622 and longitudinal and transverse dispersivities were presented in the Supporting Information  
623 (Text S4).

### 624 **3.4 Impact of ripples migration on nitrate removal**

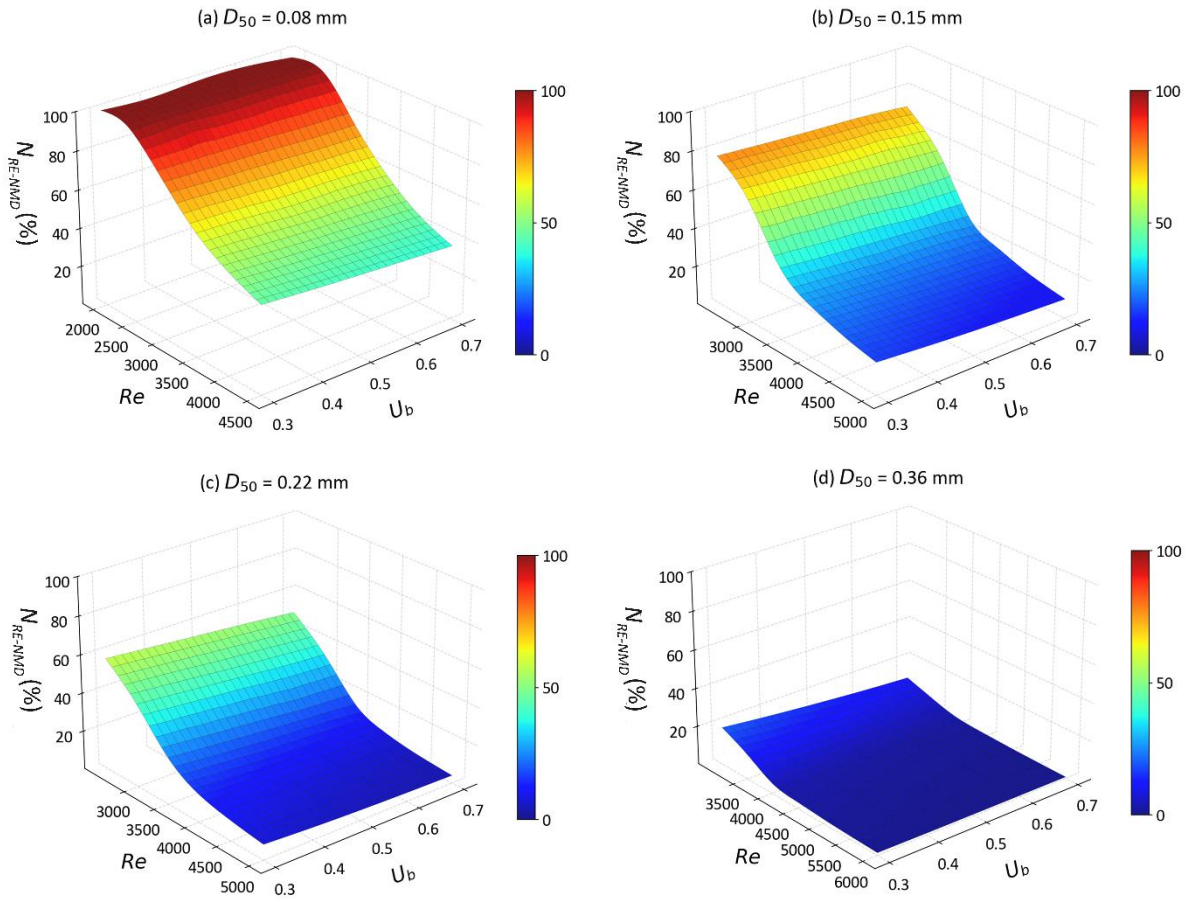
625 To assess the impact of ripple migration on the removal of s- $\text{NO}_3^-$  and g- $\text{NO}_3^-$  within  
626 domains of varying medium grain sizes, the influx of nitrate into the riverbed layer and the total  
627 reaction rate within the riverbed layer were determined.



628  
 629 **Figure 8.** The non-mixing-dependent denitrification rates ( $R_{NMD}$ ) as functions of  $U_b$  and  $Re$  for  
 630 different medium grain sizes.

631 For  $s\text{-NO}_3^-$ , the NMD denitrification rate increases in moving bedforms composed of very  
 632 fine sand ( $D_{50} = 0.08$  mm). This is likely caused by higher flow velocities driving more reactants  
 633 into the sediment, thereby enhancing denitrification in reaction-limited systems ( $Da > 2.97$ ). In  
 634 contrast, in riverbeds of fine to medium sand ( $D_{50} = 0.15\text{--}0.36$  mm) with higher permeabilities,  
 635 the rate of  $s\text{-NO}_3^-$  is negatively correlated with the mean stream velocity when the system  
 636 becomes transport-limited ( $Da < 2$ ). This is likely because  $s\text{-NO}_3^-$  travels fast along shorten  
 637 flow paths and does not undergo denitrification within the moving bedforms (Figure 6).  
 638 Additionally, the migrating bedforms enhance the delivery of  $s\text{-NO}_3^-$  into the sediment due to

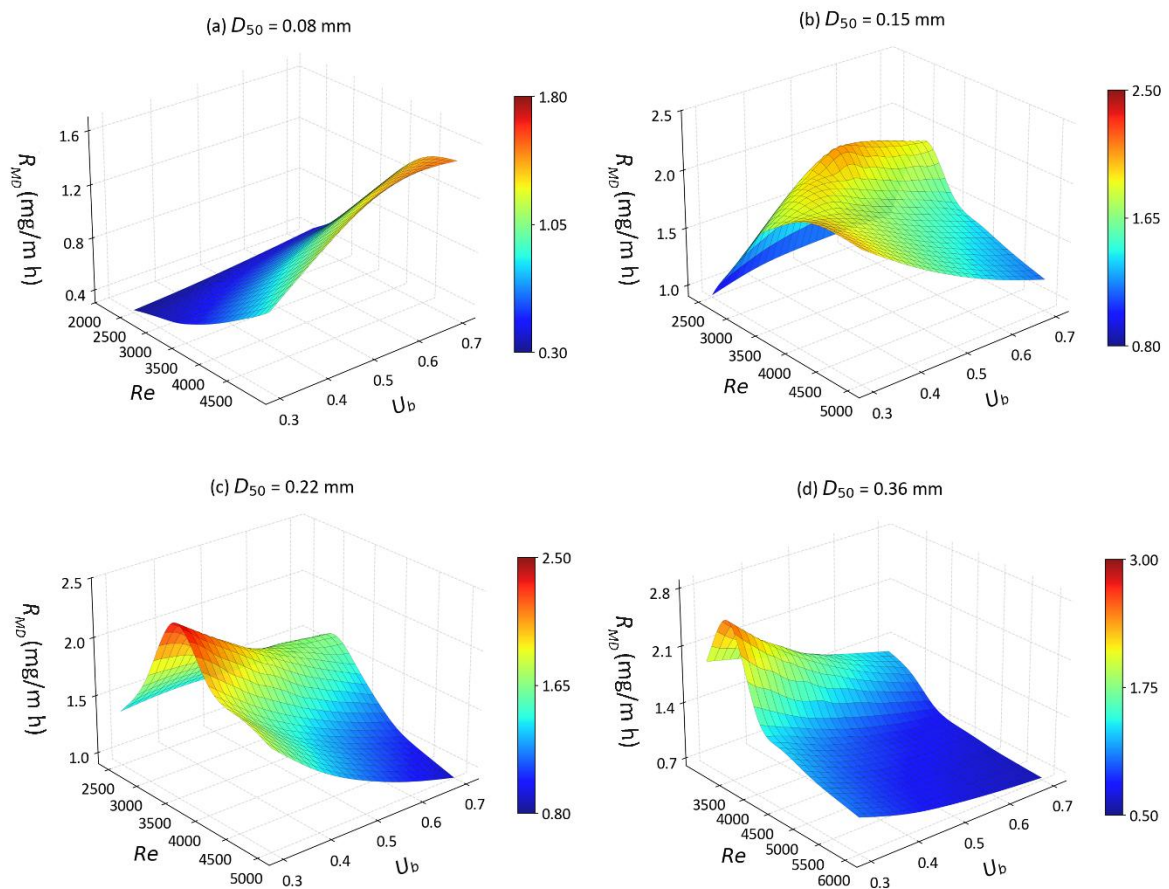
639 increased  $HEF$ . Consequently, the removal efficiency of  $s\text{-NO}_3^-$  decreases monotonically across  
 640 various medium grain sizes (Figure 9).



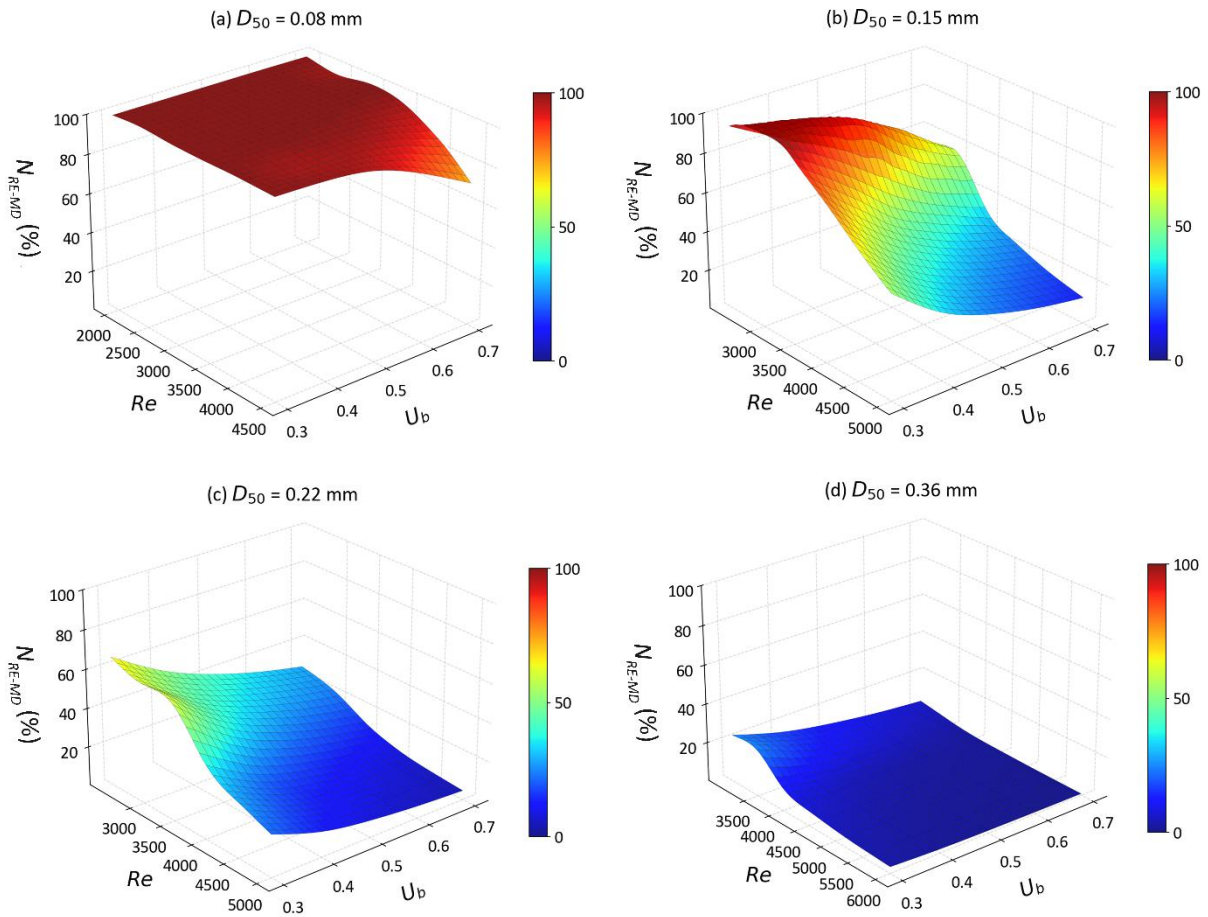
641  
 642 **Figure 9.** The removal efficiencies of stream borne nitrate ( $N_{RE-NMD}$ ) as functions of  $U_b$  and  $Re$   
 643 for different medium grain sizes.

644 For  $g\text{-NO}_3^-$ , the increase in MD denitrification is also seen for fine sandy sediments ( $D_{50} =$   
 645  $0.08\text{--}0.22$  mm) at low to medium  $Re$  (Figure 10). Compared to  $s\text{-NO}_3^-$ , the advective flow paths  
 646 and residence times of  $g\text{-NO}_3^-$  in groundwater are longer. Additionally, the enhanced mixing  
 647 dynamics between SW and GW further facilitates the occurrence of MD denitrification as the  
 648 bedforms start moving. Consequently, the reduction rate of  $g\text{-NO}_3^-$  decreases only in riverbeds  
 649 consisting of medium sand with fast bedform migration celerity ( $Re > 4000$ ), as the solute  
 650 residence time is significantly reduced. Interestingly, the rise in the MD denitrification rate

651 compensates for the increased  $g\text{-NO}_3^-$  influx in very fine sand ( $D_{50} = 0.08$  and  $0.15$  mm) at  
 652 moderate stream velocity ( $Re < 4000$ ). Most of  $g\text{-NO}_3^-$  that enters the sediment is consumed  
 653 before entering the overlying water column. For fine to medium sand riverbed, the  $g\text{-NO}_3^-$   
 654 removal efficiency decreases strongly with increasing  $Re$ . The natural protective role of the SW  
 655 and GW mixing zone in preventing nitrate-contaminated GW from entering rivers is being  
 656 hindered in fast moving bedforms (Figure 11).



657  
 658 **Figure 10.** The mixing-dependent denitrification rates ( $R_{MD}$ ) as functions of  $U_b$  and  $Re$  for  
 659 different medium grain sizes.



660  
 661 **Figure 11.** The removal efficiencies of groundwater borne nitrate ( $N_{RE-MD}$ ) as functions of  $U_b$   
 662 and  $Re$  for different medium grain sizes.

663 **4. Discussion**

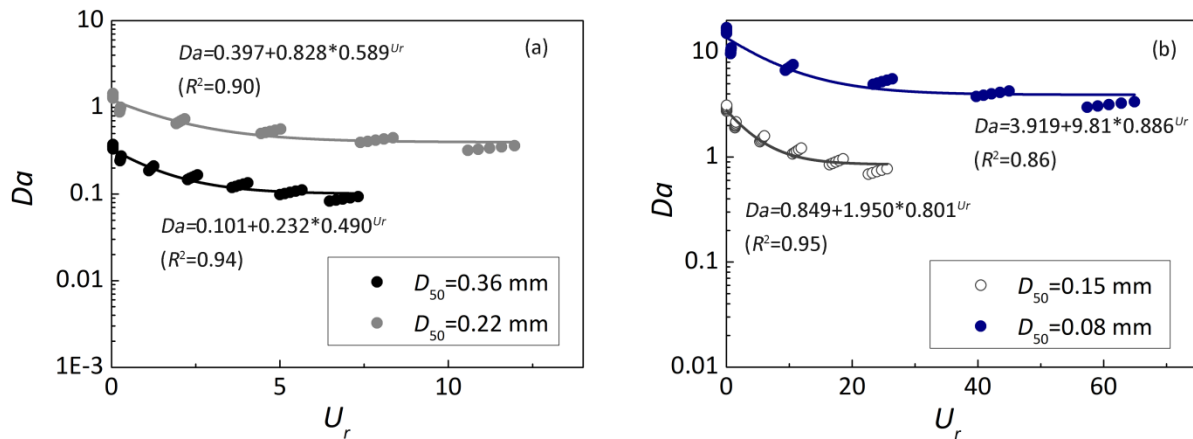
664 This study quantified the effect of bedform migration on SW and GW mixing process as  
 665 well as mixing triggered denitrification. Previous research has primarily focused on the potential  
 666 impacts of bedform migration on hyporheic exchange driven by streambed morphological  
 667 features, as well as non-mixing-dependent biogeochemical processes where reactants are  
 668 assumed to be predominantly in SW. However, such studies represent only a small subset of  
 669 possible streambed environmental conditions, focusing exclusively on specific headwater stream  
 670 conditions (Jiang et al., 2022; Kessler et al., 2015; Ping et al., 2022; Zheng et al., 2019). The

671 impact of bedform migration on the conceptual model of bedform-induced hyporheic exchange,  
672 which is influenced by GW upwelling and/or ambient lateral GW flow in the mid-stream section  
673 of lowland rivers, has received relatively less attention and examination.

674 In streams and rivers that are fed by regional GW and possess undulating bedforms, SW  
675 gets mixed with GW throughout the local hyporheic exchange process. The mixing zone  
676 exhibits a typical crescent shape along the periphery of typical hyporheic exchange cells within  
677 a stationary streambed (as reported by Fox et al., 2014; Hester et al., 2019; Nogueira et al.,  
678 2022). The sizes of the SW-GW mixing zone (e.g., thickness and area) occupy a small  
679 proportion of the whole HZ. In the immobile bedform, the thin mixing zone occupying ~5% is  
680 consistent with prior work (Hester et al., 2013; Santizo et al., 2020). However, at the onset of  
681 bedform migration, the mixing pattern, extent, and intensity of SW-GW interactions are altered.  
682 A continuous SW-GW mixing zone is formed within the ripples of the medium- to fast-moving  
683 bedform (Figure 6), and the area of mixing zone increases to approximately 10 ~ 15% at this  
684 time. Besides, the net flux of SW and GW mixing increases with stream velocity and bedform  
685 migration celerity significantly (Figure 7). As a result, bedform migration controls and  
686 determines the hotspots and magnitudes of the SW and GW mixing. The bedforms are typically  
687 assumed to be immobile potentially making underestimations of SW-GW mixing flux and  
688 mixing zone in a HZ.

689 Instead of the typical crescent-shaped MD denitrifying zone observed in stationary  
690 bedforms (Naranjo et al., 2015; Hester et al., 2014, 2019), the MD reaction zonation changes to  
691 the layer shape distributed at the fringe of the HEF cells, where mixing between SW and GW  
692 develop to a largest degree (Figure 6). Such a situation exists where the stream flows into with a

693 relative homogeneous sandy riverbed with low autochthonous organic carbon content and  
 694 encounters with nitrate enrich GW. The heterogeneous streambeds including buried  
 695 autochthonous organic matter (Sawyer, 2015; Ping et al., 2022), deposited particulate organic  
 696 particles (Drummond et al., 2017; Ping et al., 2023), and biological aggregate (Xian et al.,  
 697 2022), would complicate the hyporheic exchange process, induce the rough and irregular shapes  
 698 and boundaries of HEF cells and mixing zone, and therefore affect redox microenvironments  
 699 and biogeochemical zonations. MD denitrifying hotspot would also develop around available  
 700 sources of DOC.



702 **Figure 12.** Variation of the dimensionless Damköhler number as a function of the dimensionless  
 703 parameter  $U_r$ .

704 Previous studies have demonstrated that migrating bedforms constrains the penetration  
 705 depths of stream-borne solute, shorten their transport timescale, and reduces the removal  
 706 efficiency of stream-borne nitrate (Jiang et al., 2022; Kessler et al., 2015; Ping et al., 2022;  
 707 Zheng et al., 2019). Our findings indicate that bedform migration exerts more complex  
 708 influences on MD denitrification and groundwater-borne nitrate removal. Bedform migration  
 709 facilitates increases in the MD denitrification rate, driven by enhanced mixing flux, a higher

710 mixing proportion, and an expanded mixing zone. At the same time, it shortens the residence  
711 timescale of water and solutes, which is detrimental to the occurrence of denitrification. When  
712  $Re < 4000$  (slow to moderate stream velocities), the MD denitrification rate of moving bedforms  
713 is greater than or comparable to that of stationary bedforms; in contrast, for fast-moving  
714 bedforms ( $Re \geq 4000$ ), the MD denitrification rate decreases significantly. This is likely because  
715 the reduction in MD rate driven by a shortened transport timescale dominates over the increase  
716 caused by enhanced mixing intensity; meanwhile, at this stage ( $\sim Re 4000$ ), the mixing fraction  
717 of the total exchange flux and the extent of the mixing zone both approach plateaus. Fast-  
718 moving bedforms also reduce the HZ attenuation capacity for groundwater-borne nitrate.  
719 Notably, the  $g\text{-NO}_3^-$  removal efficiency in HZs peaks for stationary bedforms and those at the  
720 onset of migration.

721 The causes of fast-moving bedforms' negative impact on  $g\text{-NO}_3^-$  removal differ depending  
722 on the type of riverbed sediment (Figure 12). For very fine sand ( $D_{50} = 0.08$  mm), a larger  
723 celerity results in a decline in transport timescale with less impact on removal efficiency as the  
724 system is rate-limited ( $Da \gg 1$ ). For fine to medium sand riverbed ( $D_{50} = 0.15\text{--}0.36$  mm), the  
725 transport-limited situation leads to a low denitrification rate with increasing  $U_r$  but constantly  
726 decreasing  $Da$  ( $Da < 1$ ). It is important to note that the calculated reaction timescale is based on  
727 the consumption period of oxygen to a prescribed anoxic threshold. Under these conditions, the  
728 exhaustion of labile DOC would also lead to the cessation of denitrification (Zarnetske et al.,  
729 2011a, 2011b). These results demonstrate that in order to evaluate the self-purification capacity  
730 of the HZ and its function as a natural barrier mitigating groundwater contamination, riverbed  
731 sediment transport dynamics and grain size distributions need to be considered. Stabilizing

732 bedform configurations in restoration projects would enhance the natural attenuation capacity of  
733 HZs. Additionally, enhancing mixing intensity, along with extending the water residence  
734 timescale, would also facilitate the self-purification of HZs.

735 Different from previous studies that demonstrated the magnitude of NMD denitrification is  
736 often greater than that of MD denitrification (Hester et al., 2014; Trauth and Fleckenstein,  
737 2017). The results in our study show that the total reaction rate of s-NO<sub>3</sub><sup>-</sup> is smaller than that of  
738 g-NO<sub>3</sub><sup>-</sup> in mobile bedforms. This phenomenon can be attributed to the following two reasons:  
739 First, the concentration of s-NO<sub>3</sub><sup>-</sup> is one-third that of g-NO<sub>3</sub><sup>-</sup>; Second, the reaction zone is  
740 reduced by migration celerity for NMD denitrification, while the reaction zone for MD  
741 denitrification is increased in the moving riverbed. Mixing intensity increases with bedform  
742 migration, a process that facilitates MD denitrification more effectively (Hester et al., 2019;  
743 Nogueira et al., 2024; Trauth and Fleckenstein., 2017). More attention should be paid to the  
744 mixing dynamics and mixing triggered biogeochemical reactions, which is helpful to put  
745 forward appropriate stream restoration plans so as to enhance the health of the aquatic  
746 ecosystem (Hester et al., 2017; Lawrence et al., 2013).

747 The findings of this study, derived from 2D numerical models, are most directly  
748 generalizable to straight, low-curvature streams with periodic bedform distributions in riverbed  
749 sediments. In such stream systems, hyporheic exchange is dominated by streamwise-vertical  
750 flow cells, with lateral (cross-stream) hyporheic flux accounting for a small fraction of total  
751 exchange (Hu et al., 2014; Naranjo et al., 2015). Importantly, straight, low-curvature streams are  
752 prevalent in agricultural and urban downstream gaining reaches, which are characterized by  
753 relatively homogeneous sediment types (e.g., fine sands). This is consistent with the focus of our

754 study, as these reaches often face nitrate pollution challenges and depend on natural attenuation  
755 to maintain water quality (Hester et al., 2014; Trauth et al., 2017). In practice, riverbeds may  
756 exhibit far more complex three-dimensional (3D) bedform morphologies coupled with sediment  
757 heterogeneity, for example, in highly meandering streams (Gomez-Velez et al., 2017; Nogueira  
758 et al., 2024; Pescimoro et al., 2019). Future studies should establish 3D numerical model and  
759 incorporate stochastic hydraulic conductivity ( $K$ ) fields to explore how sediment heterogeneity  
760 interacts with bedform migration, evaluating whether high- $K$  hotspots enhance or reduce  
761 migration-driven mixing.

762 A critical limitation of this study is the reliance on empirical equations for bedform  
763 migration celerity. The Chezy equation (suited for flat, homogeneous sediment beds) was used  
764 to estimate the shear velocity for incipient sediment motion, with the experimentally derived  
765 empirical relationship by Coleman and Melville (1994) further adopted to account for the  
766 additional shear stress induced by ripples. The two-step approach (shear stress for particle  
767 initiation and ripple-scale form drag via empirical formulations) reproduced Wolke's (2020)  
768 results and proved useful for investigating the effects of bedform migration on hyporheic solute  
769 transport (Ahmerkamp et al., 2017; Zheng et al., 2019). We did not simulate turbulent flow over  
770 triangular bedforms nor compute shear stress via computational fluid dynamics (CFD; a  
771 numerical method that would yield more precise pressure profiles and shear stress distributions)  
772 given that the core focus of this study was to investigate how bedform migration affects  
773 hyporheic solute transport and mixing-dependent denitrification within the riverbed layer. As  
774 future work, the empirical approach should be validated using CFD simulations to enhance the  
775 accuracy of bedform-related stress and migration calculations. This validation will facilitate the

776 quantification of potential uncertainties and refine the mechanistic understanding of bedform  
777 dynamic-hyporheic zone interactions.

778 This study focuses on ripples and, more broadly, shorter-wavelength topographic roughness  
779 elements formed under low subcritical flow conditions in sandy riverbeds (Ashley, 1990;  
780 Gomez-Velez et al., 2015; Raudkivi, 1997). The undulating bedforms maintain dynamic  
781 equilibrium through geometric adjustments, with their geometry remaining unchanged as the  
782 stream velocity fluctuates within a specific range (10–30 cm/s). When stream velocities exceed  
783 this upper threshold, a condition commonly observed in fast-flowing rivers, bedform geometries  
784 can be altered, ultimately leading to bedform erosion (Boano et al., 2013; Harvey et al., 2012).  
785 This process is not accounted for in the current model. If small-scale ripples develop and merge  
786 with larger-scale ripples and dunes under high stream velocities, the removal efficiency of s-  
787  $\text{NO}_3^-$  and g- $\text{NO}_3^-$  may be enhanced due to the extended hyporheic flow paths and increased  
788 residence timescales (Harvey et al., 2012; Zomer and Hoitink, 2024). Otherwise, the removal of  
789 s- $\text{NO}_3^-$  would be highly hindered because of shorter residence time and fully oxic condition in  
790 fast moving bedforms and fast flowing rivers, while the removal of g- $\text{NO}_3^-$  would likely be less  
791 affected within the immobile streambeds.

792 The numerical models assume isotropic sediment  $K$ . In fact, natural riverbeds with small-  
793 scale bedforms (e.g., dunes and ripples) commonly exhibit strong anisotropy. For bedforms with  
794 flow-transverse crests, pore pathways parallel to the crests are relatively continuous and straight  
795 yielding high transverse  $K$ . In contrast, pathways perpendicular to the crests are highly tortuous:  
796 water here must move upward through erosional, high-porosity troughs and downward over  
797 depositional, low-porosity crests. This undulating flow path, combined with flow separation and

798 local energy losses at morphological transitions, substantially increases hydraulic resistance and  
799 lowers longitudinal  $K$  (Dallmann et al., 2020; Salehin et al., 2004). Additionally, spatial  
800 variability in bedform dimensions (e.g., increasing dune wavelength downstream) enhances this  
801 anisotropy by introducing zones of differing flow resistance along the streamwise direction  
802 (Venditti et al., 2005). Given that the model is constructed along a longitudinal section with  
803 spatially consistent, periodic bedforms, the use of an isotropic hydraulic conductivity  
804 assumption is justified. Incorporating anisotropic  $K$  is critical for accurately modeling hyporheic  
805 exchange and related biogeochemical processes in 3D heterogeneous models.

806 DNRA was not incorporated in the model, given that denitrification is typically regarded as  
807 the predominant pathway for nitrate removal, whereas DNRA plays a secondary role in nitrate  
808 transformation (Zarnetske et al., 2012). Lansdown et al. (2012) and Quick et al. (2016) have  
809 demonstrated that approximately 5% of  $^{15}\text{NO}_3^-$  tracer in river sediment incubations underwent  
810 DNRA, while 85% underwent denitrification. Nevertheless, DNRA competes with  
811 denitrification for  $\text{NO}_3^-$  and DOC as electron acceptor and donors within HZs. When an  
812 oligotrophic and/or a pristine stream infiltrate into the streambed and subsequently interact and  
813 mix with nitrate-enriched GW, the MD DNRA would not occur due to the low C/N ratio. When  
814 a eutrophication stream with higher DOC concentration, DNRA would have a greater influence  
815 in nitrate transformation because DNRA is prone to occur in  $\text{NO}_3^-$ -limited (that is DOC  
816 sufficient) conditions compared to denitrification (Zhu et al., 2023). The ammonia produced by  
817 MD DNRA would be further nitrified within the aerobic HEF cell, thereby potentially elevating  
818 the risk of nitrate pollution in SW.

819 In this model, stream velocity and upward GW flux are considered constant in the present

820 model, yet they may change in time due to storm events, tidal pumping, snowmelt, or reservoir  
821 hydro-peaking (Liu et al., 2024; Nogueira et al., 2022; Song et al., 2018). Hester et al. (2019)  
822 demonstrated that increasing surface water stage would enhance both NMD and MD  
823 denitrification. Nogueira et al. (2024) and Trauth and Fleckenstein (2017) pointed out that GW  
824 discharge events increase the magnitude of SW-GW mixing, therefore effecting the prevalence  
825 of MD denitrification. The interactions among morphological dynamics, hyporheic exchange,  
826 and biogeochemical processes under transient conditions are key areas for future research.

## 827 **5. Conclusion**

828 The numerical model developed in this study was used to simulate the interaction and  
829 mixing of upwelling groundwater with bedform-induced hyporheic flow, examining how  
830 bedform migration influences SW and GW mixing and the processing of groundwater-borne  
831 nitrate within the HZ. Our analysis quantified the mixing flux and the size of mixing zone, as  
832 well as the mixing-dependent denitrification rates and removal efficiencies across riverbed  
833 sediments characterized by varying grain sizes, stream flow velocities, and groundwater  
834 discharge fluxes. These model simulations revealed that as bedforms migrate, the SW-GW  
835 mixing zone and the associated mixing-dependent denitrification zone progressively evolve into  
836 uniform, band-like structures. When turnover dominates the hyporheic exchange process, the  
837 mixing flux increases significantly (an increase of one order of magnitude). The mixing  
838 proportion of total exchange flux and mixing zone scope also experience significant increases at  
839 the onset of migration; as stream velocity further rises, the mixing proportion (~60%) and  
840 mixing size (~10–15% of the riverbed) gradually reach plateaus. Enhanced SW-GW mixing

841 dynamics facilitates MD denitrification as bedforms begins migration; however, shortened  
842 solute residence timescales resulting from fast bedform movement limits MD denitrification  
843 occurrence. Under dynamic bedform conditions, the self-purification capacity of the HZ is  
844 reduced for fine to medium sand ( $D_{50} = 0.15\text{--}0.36$  mm), compromising its role as a natural  
845 barrier against groundwater contamination. Incorporating the identified and analyzed factors can  
846 enhance the management of riverbed sediment-associated aquatic systems, particularly for  
847 management objectives focused on removing groundwater-borne nitrate.

#### 848 **Supporting information**

849 Additional details of the model scenarios and model validation were displayed in the  
850 supporting information.

#### 851 **Data availability**

852 All raw data can be provided by the first author upon request.

#### 853 **Competing interest**

854 The authors declare that they have no conflict of interest.

#### 855 **Author contribution**

856 Conceptualization: XP, YX

857 Formal analysis: XP

858 Funding acquisition: XP, ZW, YX, SK

859 Investigation: XP, ZW

860 Methodology: XP, ZW, YX

861 Writing-original draft: XP

862 Writing-review and editing: ZW, YX, MJ, SK

863 Project administration: ZW

## 864 **Acknowledgments**

865 The work was financially supported by the National Natural Science Foundation of China  
866 (Nos. U23A2042, 42407075 and 42107089). This study was also supported by the Fellowship  
867 Program of China Postdoctoral Science Foundation under Grant Number 2025M773158 and  
868 GZC20241601, the “CUG Scholar” Scientific Research Funds at China University of  
869 Geosciences (Wuhan) (Project No.2023067), and. SK has been supported by the Royal Society  
870 (INF\R2\212060).

## 871 **Reference**

872 Ahmerkamp, S., Winter, C., Janssen, F., Kuypers, M. M., and Holtappels, M.: The impact of  
873 bedform migration on benthic oxygen fluxes, *J. Geophys. Res.: Biogeosci.* 120, 2229–  
874 2242, <https://doi.org/10.1002/2015JG003106>, 2015.

875 Ahmerkamp, S., Winter, C., Krämer, K., Beer, D. D., Janssen, F., Friedrich, J., Kuypers, M. M.  
876 M., and Holtappels, M.: Regulation of benthic oxygen fluxes in permeable sediments of the  
877 coastal ocean, *Limnol. Oceanogr.* 62(5), 1935–1954, <http://doi.org/10.1002/lno.10544>,  
878 2017.

879 Ascott, M. J., Stuart, M. E., Gooddy, D. C., Marchant, B. P., Talbot, J. C., Surridge, B. J., and  
880 Poly, D. A.: Provenance of drinking water revealed through compliance sampling,  
881 Environ. Sci.: Processes & Impacts, 21(6), 1052-1064,  
882 <https://doi.org/10.1039/C8EM00437D>, 2019.

883 Ashley, G. M.: Classification of large-scale subaqueous bedforms: A new look at an old  
884 problem-SEPM bedforms and bedding structures, J. Sediment. Res. 60(1), 160–172,  
885 <https://doi.org/10.1306/212F9138-2B24-11D7-8648000102C1865D>, 1990.

886 Azizian, M., Grant, S. B., Kessler, A. J., Cook, P. L. M., Rippy, M. A., and Stewardson, M. J.:  
887 Bedforms as biocatalytic filters: a pumping and streamline segregation model for nitrate  
888 removal in permeable sediments, Environ. Sci. Technol. 49, 10993–11002,  
889 <https://doi.org/10.1021/acs.est.5b01941>, 2015.

890 Bardini, L., Boano, F., Cardenas, M. B., Revelli, R., and Ridolfi, L.: Nutrient cycling in bedform  
891 induced hyporheic zones, Geochim. Cosmochim. Acta, 84, 47–61,  
892 <https://doi.org/10.1016/j.gca.2012.01.025>, 2012.

893 Bartholdy, J., Ernstsén, V. B., Flemming, B. W., Winter, C., Bartholomä, A., and Kroon, A.: On  
894 the formation of current ripples, Sci. Rep. 5(1), 11390, <https://doi.org/10.1038/srep11390>,  
895 2015.

896 Bear, J., and Verruijt, A.: Modeling groundwater flow and pollution. D. Reidel Publishing  
897 Company, 1998.

898 Boano, F., Harvey, J. W., Marion, A., Packman, A. I., Revelli, R., Ridolfi, L., and Wörman, A.:  
899 Hyporheic flow and transport processes: Mechanisms, models, and biogeochemical  
900 implications, *Rev. Geophys.* 52, 603–679, <https://doi.org/10.1002/2012RG000417>, 2014.

901 Boano, F., Poggi, D., Revelli, R., and Ridolfi, L.: Gravity-driven water exchange between  
902 streams and hyporheic zones, *Geophys. Res. Lett.* 36, L20402,  
903 <https://doi.org/10.1029/2009GL040147>, 2009.

904 Boano, F., Revelli, R., and Ridolfi, L.: Water and solute exchange through flat streambeds  
905 induced by large turbulent eddies, *J. Hydrol.* 402, 290–296,  
906 <https://doi.org/10.1016/j.jhydrol.2011.03.023>, 2011.

907 Boano, F., Revelli, R., and Ridolfi, L.: Modeling hyporheic exchange with unsteady stream  
908 discharge and bedform dynamics, *Water Resour. Res.* 49(7), 4089–4099,  
909 <https://doi.org/10.1002/wrcr.20322>, 2013.

910 Bottacin-Busolin, A., and Marion, A.: Combined role of advective pumping and mechanical  
911 dispersion on time scales of bed form induced hyporheic exchange, *Water Resour. Res.* 46,  
912 W08518, <https://doi.org/10.1029/2009WR008892>, 2010.

913 Boulton, A. J., Findlay, S., Marmonier, P., Stanley, E. H., and Valett, H. M.: The functional  
914 significance of the hyporheic zone in streams and rivers, *Annu. Rev. Ecol. Syst.* 29(1), 59–  
915 81, <https://doi.org/10.1146/annurev.ecolsys.29.1.59>, 1998.

916 Briggs, M. A., Lutz, L. K., Hare, D. K., and González-Pinzón, R.: Relating hyporheic fluxes,  
917 residence times, and redox-sensitive biogeochemical processes upstream of beaver dams,  
918 *Freshw. Sci.* 32, 622–641, <https://doi.org/10.1899/12-110.1>, 2013.

919 Burt, T. P., Howden, N. J. K., Worrall, F., Whelan, M. J., and Bieroza, M.: Nitrate in United  
920 Kingdom rivers: Policy and its outcomes since 1970, *Environ. Sci. Technol.*, 45(1), 175–  
921 181, <https://doi.org/10.1021/es101395s>, 2011.

922 Cardenas, M. B.: Hyporheic zone hydrologic science: A historical account of its emergence and  
923 a prospectus, *Water Resour. Res.* 51, 3601–3616, <https://doi.org/10.1002/2015WR017028>,  
924 2015.

925 Cardenas, M. B., and Wilson, J. L.: The influence of ambient groundwater discharge on  
926 exchange zones induced by current-bedform interactions, *J. Hydrol.* 331, 103–109,  
927 <https://doi.org/10.1016/j.jhydrol.2006.05.012>, 2006.

928 Cardenas, M. B., Wilson, J. L., and Haggerty, R.: Residence time of bedform-driven hyporheic  
929 exchange, *Adv. Water Resour.* 31(10), 1382–1386,  
930 <https://doi.org/10.1016/j.advwatres.2008.07.006>, 2008.

931 Coleman, S. E., and Melville, B. W.: Bed-form development, *J. Hydraul. Eng.* 120(5), 544–560,  
932 [https://doi.org/10.1061/\(ASCE\)0733-9429\(1994\)120:5\(544\)](https://doi.org/10.1061/(ASCE)0733-9429(1994)120:5(544)), 1994.

933 Conley, D. J., Paerl, H. W., Howarth, R. W., Boesch, D. F., Seitzinger, S. P., Havens, K. E.,  
934 Lancelot, C., and Likens, G. E.: Ecology: controlling eutrophication: nitrogen and  
935 phosphorus, *Science* 323, 1014–1015, <https://doi.org/10.1126/science.1167755>, 2009.

936 Dallmann, J., Phillips, C. B., Teitelbaum, Y., Sund, N., Schumer, R., Arnon, S., and Packman, A.  
937 I.: Impacts of suspended clay particle deposition on sand-bed morphodynamics, *Water*  
938 *Resour. Res.*, 56(8), e2019WR027010, <https://doi.org/10.1029/2019WR027010>, 2020.

939 Drummond, J. D., Larsen, L. G., González-Pinzón, R., Packman, A. I., and Harvey, J. W.: Fine  
940 particle retention within stream storage areas at base flow and in response to a storm event:  
941 Particle retention stream storage areas, *Water Resour. Res.* 53, 5690–5705,  
942 <https://doi.org/10.1002/2016WR020202>, 2017.

943 Elliott, A. H., and Brooks, N. H.: Transfer of nonsorbing solutes to a streambed with bed forms:  
944 Theory, *Water Resour. Res.* 33(1), 123–136, <https://doi.org/10.1029/96wr02784>, 1997.

945 Fox, A., Boano, F., and Arnon, S.: Impact of losing and gaining streamflow conditions on  
946 hyporheic exchange fluxes induced by dune-shaped bed forms, *Water Resour. Res.* 50(3),  
947 1895–1907, <https://doi.org/10.1002/2013WR014668>, 2014.

948 Fox, A., Packman, A. I., Boano, F., Phillips, C. B., and Arnon, S.: (2018). Interactions between  
949 suspended kaolinite deposition and hyporheic exchange flux under losing and gaining flow  
950 conditions, *Geophys. Res. Lett.*, 45(9), 4077–4085.  
951 <https://doi.org/10.1029/2018GL077951>, 2018.

952 Gangi, A. F.: Permeability of unconsolidated sands and porous rocks, *J. Geophys. Res.* 90(B4),  
953 3099–3104, <https://doi.org/10.1029/JB090iB04p03099>, 1985.

954 Gomez-Velez, J. D., Wilson, J. L., Cardenas, M. B., and Harvey, J. W.: Flow and residence times  
955 of dynamic river bank storage and sinuosity-driven hyporheic exchange, *Water Resour.*  
956 *Res.* 53, 8572–8595, <https://doi.org/10.1002/2017WR021362>, 2017.

957 Gomez-Velez, J. D., Harvey, J., Cardenas, M. B., and Kiel, B.: Denitrification in the Mississippi  
958 River network controlled by flow through river bedforms, *Nat. Geosci.* 8, 941–975,  
959 <https://doi.org/10.1038/NGEO2567>, 2015.

960 Gu, C., Hornberger, G. M., Herman, J. S., and Mills, A. L.: Effect of freshets on the flux of  
961 groundwater nitrate through streambed sediments, *Water Resour. Res.* 44, W05415,  
962 <https://doi.org/10.1029/2007WR006488>, 2008.

963 Harvey, J. W., Drummond, J. D., Martin, R. L., McPhillips, L. E., Packman, A. I., Jerolmack, D.  
964 J., Stonedahl, S. H., Aubeneau, A. F., Sawyer, A. H., and Larsen, L. G.:  
965 Hydrogeomorphology of the hyporheic zone: Stream solute and fine particle interactions  
966 with a dynamic streambed, *J. Geophys. Res.* 117(G4), G00N11,  
967 <https://doi.org/10.1029/2012JG002043>, 2012.

968 Hedin, L. O., Von Fischer, J. C., Ostrom, N. E., Kennedy, B. P., Brown, M. G., and Robertson,  
969 G. P.: Thermodynamic constraints on nitrogen transformations and other biogeochemical  
970 processes at soil-stream interfaces, *Ecology*, 79(2), 684–703, [https://doi.org/10.1890/0012-](https://doi.org/10.1890/0012-9658(1998)079[0684:TCONAO]2.0.CO;2)  
971 [9658\(1998\)079\[0684:TCONAO\]2.0.CO;2](https://doi.org/10.1890/0012-9658(1998)079[0684:TCONAO]2.0.CO;2), 1998.

972 Hester, E. T., Cardenas, M. B., Haggerty, R., and Sourabh, S. V. A.: The importance and  
973 challenge of hyporheic mixing, *Water Resour. Res.* 53, 3565–3575,  
974 <https://doi.org/10.1002/2016WR020005>, 2017.

975 Hester, E. T., Eastes, L. A., and Widdowson, M. A.: Effect of surface water stage fluctuation on  
976 mixing-dependent hyporheic denitrification in riverbed dunes, *Water Resour. Res.* 55,  
977 4668–4687, <https://doi.org/10.1029/2018WR024198>, 2019.

978 Hester, E. T., Young, K. I., and Widdowson, M. A.: Mixing of surface and groundwater induced  
979 by riverbed dunes: Implications for hyporheic zone definitions and pollutant reactions,  
980 *Water Resour. Res.* 49, 5221–5237, <https://doi.org/10.1002/wrcr.20399>, 2013.

981 Hester, E. T., Young, K. I., and Widdowson, M. A.: Controls on mixing-dependent  
982 denitrification in hyporheic zones induced by riverbed dunes: A steady state modeling  
983 study, *Water Resour. Res.* 50, 9048–9066, <https://doi.org/10.1002/2014WR015424>, 2014.

984 Howden, N. J. K., and Burt, T. P.: Temporal and spatial analysis of nitrate concentrations from  
985 the Frome and Piddle catchments in Dorset (UK) for water years 1978 to 2007: Evidence  
986 for nitrate breakthrough? *Sci. Total Environ.* 407(1), 507–526,  
987 <http://doi.org/10.1016/j.scitotenv.2008.08.042>, 2008.

988 Hu, H., Binley, A., Heppell, C. M., Lansdown, K., and Mao, X.: Impact of microforms on nitrate  
989 transport at the groundwater-surface water interface in gaining streams, *Adv. Water Resour.*  
990 73, 185–197, <https://doi.org/10.1016/j.advwatres.2014.07.013>, 2014.

991 Janssen, F., Cardenas, M. B., Sawyer, A. H., Dammrich, T., Krietsch, J., and de Beer, D.: A  
992 comparative experimental and multiphysics computational fluid dynamics study of coupled  
993 surface-subsurface flow in bed forms, *Water Resour. Res.* 48(8), W08514,  
994 <https://doi.org/10.1029/2012WR011982>, 2012.

995 Jiang, Q., Liu, D., Jin, G., Tang, H., Wei, Q., and Xu, J.: N<sub>2</sub>O dynamics in the hyporheic zone  
996 due to ripple migration, *J. Hydrol.* 610, 127891,  
997 <https://doi.org/10.1016/j.jhydrol.2022.127891>, 2022.

998 Kessler, A. J., Cardenas, M. B., and Cook, P. L. M.: The negligible effect of bed form migration  
999 on denitrification in hyporheic zones of permeable sediments, *J. Geophys. Res.: Biogeosci.*  
1000 120, 538–548, <https://doi.org/10.1002/2014JG002852>, 2015.

1001 Krause, S., Abbott, B. W., Baranov, V., Bernal, S., Blaen, P., Datry, T., Drummond, J.,  
1002 Fleckenstein, J. H., Velez, J. G., Hannah, D. M., Knapp, J. L. A., Kurz, M., Lewandowski,  
1003 J., Martí, E., Mendoza-Lera, C., Milner, A., Packman, A., Pinay, G., Ward, A. S., and  
1004 Zarnetzke, J. P.: Organizational principles of hyporheic exchange flow and biogeochemical  
1005 cycling in river networks across scales, *Water Resour. Res.* 58 (3), e2021WR029771,  
1006 <https://doi.org/10.1029/2021WR029771>, 2022.

1007 Krause, S., Heathwaite, L., Binley, A., and Keenan, P.: Nitrate concentration changes at the  
1008 groundwater-surface water interface of a small Cumbrian River, *Hydrol. Processes*, 23,  
1009 2195–2211, <https://doi.org/10.1002/hyp.7213>, 2009.

1010 Krause, S., Tecklenburg, C., Munz, M., and Naden, E.: Streambed nitrogen cycling beyond the  
1011 hyporheic zone: Flow controls on horizontal patterns and depth distribution of nitrate and  
1012 dissolved oxygen in the upwelling groundwater of a lowland river, *J. Geophys. Res.:*  
1013 *Biogeosciences*, 118, 54–67, <https://doi.org/10.1029/2012JG002122>, 2013.

1014 Lansdown, K., Heppell, C. M., Dossena, M., Ullah, S., Heathwaite, A. L., Binley, A., Zhang, H.,  
1015 Trimmer, M., 2014. Fine-Scale in situ measurement of riverbed nitrate production and  
1016 consumption in an armored permeable riverbed, *Environ. Sci. Technol.* 48 (8), 4425–4434,  
1017 <https://doi.org/10.1021/es4056005>, 2014.

1018 Lansdown, K., Heppell, C. M., Trimmer, M., Binley, A., Heathwaite, A. L., Byrne, P., and  
1019 Zhang, H.: The interplay between transport and reaction rates as controls on nitrate  
1020 attenuation in permeable, streambed sediments, *J. Geophys. Res. Biogeosci.* 120, 1093–  
1021 1109, <http://doi.org/10.1002/2014JG002874>, 2015.

1022 Lansdown, K., Trimmer, M., Heppell, C. M., Sgouridis, F., Ullah, S., Heathwaite, L., Binley, A.,  
1023 and Zhang, H.: Characterization of the key pathways of dissimilatory nitrate reduction and  
1024 their response to complex organic substrates in hyporheic sediments, *Limnol. Oceanogr.* 57  
1025 (2), 387–400, <https://doi.org/10.4319/lo.2012.57.2.0387>, 2012.

1026 Lawrence, J. E., Skold, M. E., Hussain, F. A., Silverman, D. R., Resh, V. H., Sedlak, D. L.,  
1027 Luthy, R. G., and McCray, J. E.: Hyporheic zone in urban streams: A review and  
1028 opportunities for enhancing water quality and improving aquatic habitat by active  
1029 management, *Environ. Eng. Sci.* 30, 480–501, <https://doi.org/10.1089/ees.2012.0235>, 2013.

1030 Liu, F., Ding, Y., Liu, J., Latif, J., Qin, J., Tian, S., Sun, S., Guan, B., Zhu, K., and Jia, H.: The  
1031 effect of redox fluctuation on carbon mineralization in riparian soil: An analysis of the  
1032 hotspot zone of reactive oxygen species production, *Water Res.* 265, 122294,  
1033 <https://doi.org/10.1016/j.watres.2024.122294>, 2024.

1034 Liu, Y., Liu, C., Nelson, W. C., Shi, L., Xu, F., Liu, Y., ... and Zachara, J. M.: Effect of water  
1035 chemistry and hydrodynamics on nitrogen transformation activity and microbial  
1036 community functional potential in hyporheic zone sediment columns, *Environ. Sci.*  
1037 *Technol.*, 51(9), 4877–4886, <https://doi.org/10.1021/acs.est.6b05018>, 2017.

1038 Marzadri, A., Tonina, D., and Bellin, A.: Morphodynamic controls on redox conditions and on  
1039 nitrogen dynamics within the hyporheic zone: application to gravel bed rivers with  
1040 alternate-bar morphology, *J. Geophys. Res.: Biogeosci.* 117, 184–189,  
1041 <https://doi.org/10.1029/2012JG001966>, 2012.

- 1042 Monod, J.: The growth of bacteria cultures, *Annu. Rev. Microbiol.*, 3, 371–394,  
1043 <https://doi.org/10.1146/annurev.mi.03.100149.002103>, 1949.
- 1044 Munz, M., Krause, S., Tecklenburg, C., and Binley, A.: Reducing monitoring gaps at the aquifer-  
1045 river interface by modelling groundwater-surface water exchange flow patterns, *Hydrol.*  
1046 *Processes*, 25, 3547–3562, <https://doi.org/10.1002/hyp.8080>, 2011.
- 1047 Naranjo, R. C., Niswonger, R. G., and Davis, C. J.: Mixing effects on nitrogen and oxygen  
1048 concentrations and the relationship to mean residence time in a hyporheic zone of a riffle-  
1049 pool sequence, *Water Resour. Res.* 51(9), 7202–7217,  
1050 <https://doi.org/10.1002/2014WR016593>, 2015.
- 1051 Nogueira, G. E. H., Partington, D., Heidbuchel, I., and Fleckenstein, J. H.: Combined effects of  
1052 geological heterogeneity and discharge events on groundwater and surface water mixing, *J.*  
1053 *Hydrol.* 638, 131467, <https://doi.org/10.1016/j.jhydrol.2024.131467>, 2024.
- 1054 Nogueira, G. E. H., Schmidt, C., Brunner, P., Graeber, D., and Fleckenstein, J. H.: Transit-time  
1055 and temperature control the spatial patterns of aerobic respiration and denitrification in the  
1056 riparian zone, *Water Resour. Res.* 57 (12), e2021WR030117,  
1057 <https://doi.org/10.1029/2021WR030117>, 2021.
- 1058 Nogueira, G. E. H., Schmidt, C., Partington, D., Brunner, P., and Fleckenstein, J. H.:  
1059 Spatiotemporal variations in water sources and mixing spots in a riparian zone, *Hydrol.*  
1060 *Earth Syst. Sci.*, 26 (7), 1883–1905, <https://doi.org/10.5194/hess-26-1883-2022>, 2022.

- 1061 Ocampo, C. J., Oldham, C. E., and Sivapalan, M.: Nitrate attenuation in agricultural catchments:  
1062 shifting balances between transport and reaction, *Water Resour. Res.* 42(1), 85–88,  
1063 <https://doi.org/10.1029/2004WR003773>, 2006.
- 1064 Peleg, E., Teitelbaum, Y., and Arnon, S.: Exploring the influence of sediment motion on  
1065 microplastic deposition in streambeds, *Water Res.* 249, 120952,  
1066 <https://doi.org/10.1016/j.watres.2023.120952>, 2024.
- 1067 Pescimoro, E., Boano, F., Sawyer, A. H., and Soltanian, M. R.: Modeling influence of sediment  
1068 heterogeneity on nutrient cycling in streambeds, *Water Resour. Res.* 55,  
1069 <https://doi.org/10.1029/2018WR024221>, 2019.
- 1070 Ping, X., Xian, Y., and Jin, M.: Influence of bedform migration on nitrate reduction in hyporheic  
1071 zones of heterogeneous sediments, *Water Resour. Res.* 58, e2022WR033258,  
1072 <https://doi.org/10.1029/2022WR033258>, 2022.
- 1073 Ping, X., Xian, Y., and Jin, M.: Effect of particulate organic carbon deposition on nitrate  
1074 reduction in the hyporheic zone, *Water Resour. Res.* 59, e2022WR034253,  
1075 <https://doi.org/10.1029/2022WR034253>, 2023.
- 1076 Precht, E., Franke, U., Polerecky, L., and Huttel, M.: Oxygen dynamics in permeable sediments  
1077 with wave-driven pore water exchange, *Limnol. Oceanogr.* 49(3), 693–705,  
1078 <https://doi.org/10.2307/3597786>, 2004.
- 1079 Quick, A. M., Reeder, W. J., Farrell, T. B., Tonina, D., Feris, K. P., and Benner, S. G.: Controls  
1080 on nitrous oxide emissions from the hyporheic zones of streams, *Environ. Sci. Technol.* 50  
1081 (21), 11491–11500, <https://doi.org/10.1021/acs.est.6b02680>, 2016.

1082 Raudkivi, A. J.: Ripples on stream bed, *J. Hydraul. Eng.* 123(1), 58–64,  
1083 [https://doi.org/10.1061/\(ASCE\)0733-9429\(1997\)123:1\(58\)](https://doi.org/10.1061/(ASCE)0733-9429(1997)123:1(58)), 1997.

1084 Reeder, W. J., Quick, A. M., Farrell, T. B., Benner, S. G., Feris, K. P., and Tonina, D.: Spatial  
1085 and temporal dynamics of dissolved oxygen concentrations and bioactivity in the hyporheic  
1086 zone, *Water Resour. Res.* 54, 2112–2128, <https://doi.org/10.1002/2017WR021388>, 2018.

1087 Risse-Buhl, U., Arnon, S., Bar-Zeev, E., Oprei, A., Packman, A. I., Peralta-Maraver, I.,  
1088 Robertson, A., Teitelbaum, Y., and Mutz, M.: Streambed migration frequency drives  
1089 ecology and biogeochemistry across spatial scales, *Wiley Interdiscip. Rev.: Water*, 10.  
1090 <https://doi.org/10.1002/wat2.1632>, 2023.

1091 Rivett, M. O., Buss, S. R., Morgan, P., Smith, J. W. N., and Bemment, C. D.: Nitrate attenuation  
1092 in groundwater: A review of biogeochemical controlling processes, *Water Res.* 42, 4215–  
1093 4232, <http://doi.org/10.1016/j.watres.2008.07.020>, 2008.

1094 Roche, K. R., Blois, G., Best, J. L., Christensen, K. T., Aubeneau, A. F., and Packman, A. I.:  
1095 Turbulence links momentum and solute exchange in coarse-grained streambeds, *Water*  
1096 *Resour. Res.* 54, 3225–3242, <https://doi.org/10.1029/2017WR021992>, 2018.

1097 Roche, K. R., Li, A., Bolster, D., Wagner, G. J., and Packman, A. I.: Effects of turbulent  
1098 hyporheic mixing on reach-scale transport, *Water Resour. Res.* 55,  
1099 <https://doi.org/10.1029/2018WR023421>, 2019.

1100 Rouse, J. D., Bishop, C. A., and Struger, J.: Nitrogen pollution: an assessment of its threat to  
1101 amphibian survival, *Environ. Health Perspect.* 107, 799–803,  
1102 <https://doi.org/10.1289/ehp.99107799>, 1999.

1103 Salehin, M., Packman, A. I., and Paradis, M.: Hyporheic exchange with heterogeneous  
1104 streambeds: Laboratory experiments and modeling, *Water Resour. Res.* 40, W11504,  
1105 <http://doi.org/10.1029/2003WR002567>, 2004.

1106 Santizo, K. Y., Widdowson, M. A., and Hester, E. T.: Abiotic mixing-dependent reaction in a  
1107 laboratory simulated hyporheic zone, *Water Resour. Res.* 56 (9), e2020WR027090,  
1108 <https://doi.org/10.1029/2020WR027090>, 2020.

1109 Sawyer, A. H.: Enhanced removal of groundwater-borne nitrate in heterogeneous aquatic  
1110 sediments, *Geophys. Res. Lett.* 42(2), 403–410, <https://doi.org/10.1002/2014GL062234>,  
1111 2015.

1112 Schindler, R. J., Parsons, D. R., Ye, L., Hope, J. A., Baas, J. H., Peakall, J., Manning, A. J.,  
1113 Aspden, A. J., Malarkey, J., and Simmons, S.: Sticky stuff: redefining bedform prediction  
1114 in modern and ancient environments, *Geology*, 43, 399–402,  
1115 <https://doi.org/10.1130/G36262.1>, 2015.

1116 Schulz, H., Teitelbaum, Y., Lewandowski, J., Singer, G. A., and Arnon, S.: Moving bedforms  
1117 control CO<sub>2</sub> production and distribution in sandy river sediments, *J. Geophys. Res.:*  
1118 *Biogeosci.* 128, e2022JG007156, <https://doi.org/10.1029/2022JG007156>, 2023.

1119 Shelley, F., Klaar, M., Krause, S., and Trimmer, M.: Enhanced hyporheic exchange flow around  
1120 woody debris does not increase nitrate reduction in a sandy streambed, *Biogeochem.* 136  
1121 (3), 353–372, <https://doi.org/10.1007/s10533-017-0401-2>, 2017.

1122 Soulsby, R.: Dynamics of marine sands: a manual for practical applications, *Oceanogr. Lit. Rev.*,  
1123 9, 947, 1997.

- 1124 Song, X., Chen, X., Stegen, J., Hammond, G., Song, H.-S., Dai, H., Graham, E., and Zachara, J.  
1125 M.: Drought conditions maximize the impact of high-frequency flow variations on thermal  
1126 regimes and biogeochemical function in the hyporheic zone, *Water Resour. Res.* 54 (10),  
1127 7361–7382, <https://doi.org/10.1029/2018WR022586>, 2018.
- 1128 Stelzer, R. S., and Bartsch, L. A.: Nitrate removal in deep sediments of a nitrogen-rich river  
1129 network: A test of a conceptual model, *J. Geophys. Res.* 117, G02027,  
1130 <http://doi.org/10.1029/2012JG001990>, 2012.
- 1131 Tonina, D., and Buffington, J. M.: Hyporheic exchange in gravel bed rivers with pool-riffle  
1132 morphology: Laboratory experiments and three-dimensional modeling, *Water Resour. Res.*  
1133 43, W01421, <https://doi.org/10.1029/2005WR004328>, 2007.
- 1134 Trauth, N., and Fleckenstein, J. H.: Single discharge events increase reactive efficiency of the  
1135 hyporheic zone, *Water Resour. Res.* 53(1), 779–798.  
1136 <https://doi.org/10.1002/2016WR019488>, 2017.
- 1137 Trauth, N., Musolff, A., Knller, K., Kaden, U. S., and Fleckenstein, J. H.: River water infiltration  
1138 enhances denitrification efficiency in riparian groundwater, *Water Resour.* 130, 185–199,  
1139 <https://doi.org/10.1016/j.watres.2017.11.058>, 2017.
- 1140 Venditti, J. G., Church, M., and Bennett, S. J.: Morphodynamics of small-scale superimposed  
1141 sand waves over migrating dune bed forms, *Water Resour. Res.*, 41(10), W10423,  
1142 <https://doi.org/10.1029/2004WR003461>, 2005.

1143 Wolke, P., Teitelbaum, Y., Deng, C., Lewandowski, J., and Arnon, S.: Impact of bed form  
1144 celerity on oxygen dynamics in the hyporheic zone, *Water*, 12(1), 62,  
1145 <https://doi.org/10.3390/w12010062>, 2020.

1146 Wondzell, S. M., LaNier, J., Haggerty, R., Woodsmith, R. D., and Edwards, R. T.: Changes in  
1147 hyporheic exchange flow following experimental wood removal in a small, low-gradient  
1148 stream, *Water Resour. Res.* 45, <https://doi.org/10.1029/2008WR007214>, 2009.

1149 Woessner, W.: Stream and fluvial plain ground water interactions: rescaling hydrogeologic  
1150 thought, *Ground Water*, 38(3), 15–25, <https://doi.org/10.1111/j.1745-6584.2000.tb00228.x>,  
1151 2000.

1152 Wu, L., Gomez-Velez, J. D., Li, L., and Carroll, K. C.: The fragility of bedform-induced  
1153 hyporheic zones: Exploring impacts of dynamic groundwater table fluctuations, *Water*  
1154 *Resour. Res.* 60, e2023WR036706, <https://doi.org/10.1029/2023WR036706>, 2024.

1155 Xian, Y., Jin, M., Zhan, H., and Liang, X.: Permeable biofilms can support persistent hyporheic  
1156 anoxic microzones, *Geophys. Res. Lett.* 49, e2021GL096948,  
1157 <https://doi.org/10.1029/2021GL096948>, 2022.

1158 Zarnetske, J. P., Haggerty, R., Wondzell, S. M., and Baker, M. A.: Dynamics of nitrate  
1159 production and removal as a function of residence time in the hyporheic zone, *J. Geophys.*  
1160 *Res. Biogeosci.* 116, G01025, <https://doi.org/10.1029/2010JG001356>, 2011a.

1161 Zarnetske, J. P., Haggerty, R., Wondzell, S. M., and Baker, M. A.: Labile dissolved organic  
1162 carbon supply limits hyporheic denitrification, *J. Geophys. Res. Biogeosci.* 116, G04036,  
1163 <https://doi.org/10.1029/2011JG001730>, 2011b.

- 1164 Zarnetske, J. P., Haggerty, R., Wondzell, S. M., Bokil, V. A., and González-Pinzón, R.: Coupled  
1165 transport and reaction kinetics control the nitrate source-sink function of hyporheic zones,  
1166 Water Resour. Res. 48 (11), 1–15, <https://doi.org/10.1029/2012WR011894>, 2012.
- 1167 Zheng, L., Cardenas, M. B., Wang, L., and Mohrig, D.: Ripple effects: Bed form  
1168 morphodynamics cascading into hyporheic zone biogeochemistry, Water Resour. Res. 55,  
1169 7320–7342, <https://doi.org/10.1029/2018WR023517>, 2019.
- 1170 Zhu, Y., Dai, H., and Yuan, S.: The competition between heterotrophic denitrification and  
1171 DNRA pathways in hyporheic zone and its impact on the fate of nitrate, J. Hydrol. 626:  
1172 130175, <https://doi.org/10.1016/j.jhydrol.2023.130175>, 2023.
- 1173 Zomer, J. Y., and Hoitink, A. J. F.: Evidence of secondary bedform controls on river dune  
1174 migration, Geophys. Res. Lett. 51(15), <https://doi.org/10.1029/2024GL109320>, 2024.